

RESEARCH ARTICLE

10.1002/2013JB010444

Key Points:

- Time-independent compaction of sands controls porosity during sediment burial
- Compaction experiments on sands were combined with a microphysical model
- Compaction seems to be controlled by contact asperity amplitude of the grains

Correspondence to:

S. J. T. Hangx,
S.J.T.Hangx@uu.nl

Citation:

Brzesowsky, R. H., C. J. Spiers, C. J. Peach, and S. J. T. Hangx (2014), Time-independent compaction behavior of quartz sands, *J. Geophys. Res. Solid Earth*, 119, 936–956, doi:10.1002/2013JB010444.

Received 16 JUN 2013

Accepted 3 JAN 2014

Accepted article online 8 JAN 2014

Published online 13 FEB 2014

Time-independent compaction behavior of quartz sands

R. H. Brzesowsky^{1,2}, C. J. Spiers¹, C. J. Peach¹, and S. J. T. Hangx^{1,3}

¹HPT-laboratory, Faculty of Geosciences, Utrecht University, Utrecht, Netherlands, ²Now at Philips Research, Eindhoven, Netherlands, ³Shell Global Solutions, Rijswijk, Netherlands

Abstract Mechanisms such as grain rearrangement, coupled with elastic deformation and grain breakage, are believed to play an important role in the time-independent compaction of sands, controlling porosity and permeability reduction during burial of clastic sediments and during depletion of highly porous reservoir sandstones. We performed uniaxial compaction experiments on sands at room temperature to systematically investigate the effect of loading history, loading rate, grain size, initial porosity, and chemical environment on compaction. Acoustic emission counting and microstructural methods were used to verify the microphysical compaction mechanisms operating. All tests showed quasi-elastic loading behavior accompanied by permanent deformation, involving elastic grain contact distortion, particle rearrangement, and grain failure. Loading history, grain size, and initial porosity significantly affected stress-strain behavior, with increasing grain size and initial porosity promoting compaction. In contrast, chemical environment and loading rate had little effect. The results formed the basis for a microphysical model aimed at explaining the observed compaction behavior. Two extreme cases were modeled: (I) a pack of spherical grains with a distributed flaw size at failure and (II) a pack of nonspherical grains with a constant mean crack size at failure but a distributed effective surface radius of curvature characterizing distributed contact asperity amplitudes. The best agreement with the grain-size- and porosity-dependent trends observed in our experiments was obtained using case (II) of the model. Combining our experimental and modeling results, it was inferred that a grain-size-dependent departure from sphericity of the grains exerts a key control on the compaction behavior of sands.

1. Introduction

Time-independent volumetric compaction of sands (i.e., instantaneous compaction for which creep effects are negligible), by mechanisms such as grain rearrangement, grain rotation, intergranular sliding, elastic deformation, and grain breakage, plays an important role in determining porosity and permeability reduction during burial of clastic sediments [Antonellini *et al.*, 1994; Burley, 1986; Chester *et al.*, 2004; Chuhan *et al.*, 2002, 2003; Donaldson *et al.*, 1995; Wilson and McBride, 1988]. In general, these mechanisms operate alongside time-dependent processes like pressure solution [Groshong, 1988; Milliken, 1994; Niemeijer *et al.*, 2002; Onasch, 1994; Schutjens, 1991; Visser *et al.*, 2012].

While pressure solution typically dominates the final stages of burial-driven compaction, time-independent compaction mechanisms usually dominate in the early stages. In poorly consolidated, highly porous sands and sandstones, for example, grain rotation, intergranular sliding, grain failure, and pore collapse often lead to significant reduction in porosity through the development of compaction bands [Antonellini *et al.*, 1994; Aydin *et al.*, 2006; Cilona *et al.*, 2012; Eichhubl *et al.*, 2010; Mollema and Antonellini, 1996; Rustichelli *et al.*, 2012; Skurtveit *et al.*, 2013; Wong and Baud, 2012]. The reduced porosity and permeability of such bands can produce natural barriers to flow within reservoir rocks [Baud *et al.*, 2012; Fossen *et al.*, 2011; Zhu *et al.*, 1997]. Similarly, time-independent compaction processes operating in highly porous water- and hydrocarbon-bearing clastic reservoirs can exert important controls on production-related reservoir deformation, subsidence, and induced seismicity [Doornhof *et al.*, 2006; Hettema *et al.*, 2002; Schutjens, 1991; Segall, 1992; Zoback and Byerlee, 1976]. Compaction phenomena are also critical in determining the response of oil sands to cyclic steam injection for stimulation purposes [Wong *et al.*, 1993]. Last but not least, time-independent compaction effects must also occur in fault gouges developed in seismically active faults. Here, such effects may play a key role in controlling both dynamic and static changes in the fluid transport and strength properties of the fault, through coupling with changes in the in situ effective stress state [King and Sammis, 1992; Marone and Scholz, 1989; Rice, 1992].

Due to its practical importance, a great deal of work has been done on compaction of sands and other granular materials, from both experimental and theoretical points of view. Experimental studies have been carried out on the time-independent compaction behavior of sands under both one-dimensional and hydrostatic compression conditions [e.g., *Chuhan et al.*, 2002, 2003; *Hangx et al.*, 2010; *Karner et al.*, 2005; *Lambe and Whitman*, 1979]. These typically show nonlinear stress-strain behavior with part of the deformation being elastic, due to quasi-Hertzian grain contact distortion, and part being permanent, probably due to rolling- or sliding-induced grain rearrangement at low applied stresses [*Brzesowsky*, 1995; *Ko and Scott*, 1967; *Lambe and Whitman*, 1979; *Roberts and de Souza*, 1958]. At higher stresses, grain crushing enhances further compaction, as revealed by grain-size reduction and sometimes audible acoustic emissions [*Brzesowsky*, 1995; *Gill et al.*, 1990; *Hangx et al.*, 2010; *Karner et al.*, 2005; *Lambe and Whitman*, 1979; *Roberts and de Souza*, 1958]. The role of grain fracturing is further supported by microstructural observations on sands deformed at high stresses, which typically exhibit intragranular and transgranular cracks radiating from points of grain contact [*Borg et al.*, 1960; *Brzesowsky*, 1995; *Hangx et al.*, 2010; *Maxwell*, 1960]. In general, the overall compressibility of sands, including elastic and permanent effects, is known to be favored by higher initial porosity, increasing grain angularity, increasing grain size and size uniformity, and decreasing intrinsic grain strength [*Borg et al.*, 1960; *Brzesowsky*, 1995; *Chuhan et al.*, 2002, 2003; *Hangx et al.*, 2010; *Karner et al.*, 2005; *Lee and Farhoomand*, 1967; *Vesic and Clough*, 1968; *Zoback and Byerlee*, 1976]. This is because higher initial porosity, increased grain angularity, and larger grain size lead to higher stress concentrations at grain-to-grain contacts [e.g., see *Chuhan et al.*, 2002, 2003; *Hangx et al.*, 2010]. Similarly, increased size uniformity means a narrower grain-size range, again leading to higher contact stresses due to a lower coordination number [*Chuhan et al.*, 2003]. At the same time, decreasing grain strength means that grains will be more prone to failure and hence rearrangement at lower applied stresses.

However, many of these effects have not been investigated systematically and are not well understood at the level of a quantitative mechanism-based description. Theoretical and numerical modeling studies of the compaction of granular media have been largely based on the consideration of the elastic contact distortion of a 2-D or 3-D array of spherical grains, in most cases allowing for intergranular frictional sliding rearrangements only and focusing on nonhydrostatic states of stress [e.g., see *Shen et al.*, 1992; *Thornton*, 1993; *Mehta* 1994]. In more recent discrete element models (DEMs), sand particles are represented by circular disks, which shrink as a result of breakage [*Wang et al.*, 2008], or as conglomerates of bonded microspheres, whereby grain failure is modeled by debonding between these microspheres [*Cheng et al.*, 2003; *Harirechi and McDowell*, 2003]. These DEM models are capable of capturing and simulating the key features of failure mode and damage evolution caused by grain crushing and pore collapse. Several attempts have been made to incorporate the effects of brittle grain crushing via a simplified approach allowing for particle failure [*Issa and Nelson*, 1989; *Liu et al.*, 1993; *Ouwerkerk*, 1991; *Papamichos et al.*, 1993]. However, in these models grain failure is described only in threshold strength terms. As such, microphysical aspects of grain failure have not been incorporated and the important effects of, for example, grain size on stress-strain behavior, widely observed in compaction experiments on granular materials [*Hangx et al.*, 2010; *Liteanu et al.*, 2012; *Zhang et al.*, 1990a; *Zhang et al.*, 1990b; *Zhu et al.*, 1997], have not been explained.

In this paper, we report on both experimental and theoretical aspects of the compaction behavior of sands. Uniaxial (i.e., one-dimensional, oedometer-type) compaction experiments were performed to systematically investigate the effect of loading history, loading rate, grain size, initial porosity, and chemical environment on the compaction behavior of sands at room temperature and applied effective stress equivalent to burial depths of 2–3 km. Acoustic emission (AE) detection and microstructural methods were used to gain insight into the microphysical compaction mechanisms operative. Results were compared with a simple microphysical model for the compaction of sands, developed assuming a Hertzian contact plus LEFM (linear elastic fracture mechanics) model, allowing for elastic contact distortion plus grain contact crushing [*Brzesowsky et al.*, 2011]. Making use of results drawn from the single-grain crushing experiments reported by *Brzesowsky et al.* [2011], the model satisfactorily accounts for the grain-size effect observed in our compaction tests on sands in terms of a grain-size dependence of grain strength, reflecting a grain-size-dependent departure from an idealized spherical grain shape.

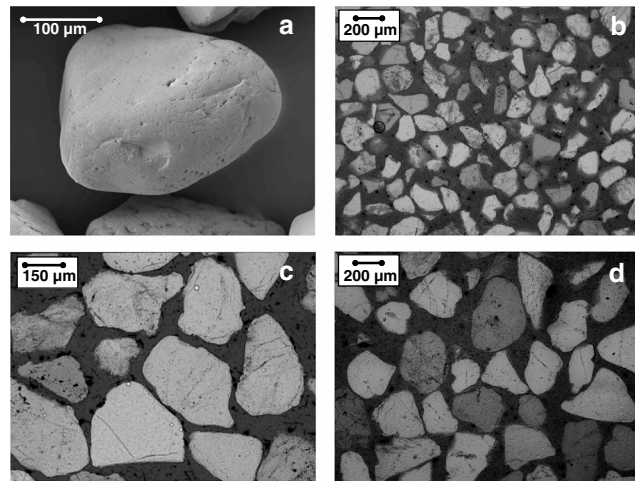


Figure 1. Micrographs of the Heksenberg starting material. (a) SEM micrograph showing a close-up of one of the grains (grain-size fraction $275 \pm 25 \mu\text{m}$), showing that most sand grains appear as subrounded and show a generally smooth surface with patches of pits, grooves/scratches, and depressions created by broken out pieces. (b) Optical microscopy micrograph of grain-size fraction $196 \pm 16 \mu\text{m}$. (c) Detailed optical microscopy micrograph of grain-size fraction $275 \pm 25 \mu\text{m}$, showing the “closed” intragranular cracks and inclusion trails. (d) Optical microscopy micrograph of grain-size fraction $378 \pm 22 \mu\text{m}$. Note that grain roundness, and hence the radius of curvature of a grain asperity, increases with increasing grain size [see Brzesowsky *et al.*, 2011].

1. Load-cycling experiments, performed on dry samples by cycling the applied (effective) stress from 0.24 MPa to a maximum of 30 MPa (equivalent to a burial depth or reservoir depth of 2.5–3 km) over a number of cycles. In all, 37 such tests were performed using three different grain-size batches ($196 \pm 16 \mu\text{m}$, $275 \pm 25 \mu\text{m}$, and $378 \pm 22 \mu\text{m}$), at loading rates of 3.9–390 MPa/h.
2. Direct loading experiments performed on fluid-flooded samples, by directly loading the sample at a constant loading rate of 5495 MPa/h, from a stress of 0.24 MPa up to 30 MPa. These seven tests were performed on a fixed grain-size batch ($d = 275 \pm 25 \mu\text{m}$), with the aim of assessing the effect of chemical environment on stress-strain behavior.

2.1. Sample Material and Pore Fluid Preparation

The sand used in our present experiments was the same as that used by Brzesowsky *et al.* [2011] and was obtained from fresh samples taken from the Heksenberg Formation at the Beaujean quarry near Heerlen, Netherlands. X-ray diffraction analysis and inductively coupled plasma emission spectroscopy (ICP-ES) measurements indicate a quartz content of $> 99 \text{ wt } \%$, with zircon and Na-rich feldspar present as the principal trace minerals. In reflected light, some sand grains ($< 0.5\%$) show a thin surface coating of iron oxide/hydroxide, supported by 0.02 wt% Fe detected in ICP-ES measurements. Scanning electron microscopy (SEM) showed that most sand grains are subrounded and have a generally smooth surface with local, pitted patches (diameter $\sim 20\text{--}50 \mu\text{m}$), characterized by rounded and triangular pits (dimension $\sim 5\text{--}15 \mu\text{m}$). Grooves (dimension $\sim 5 \times 50 \mu\text{m}$) and depressions (dimension $\sim 50 \mu\text{m}$) apparently corresponding to spalled-out fragments are also locally present (see Figure 1a). With reference to Figures 1b–1d (sieved fraction), thin section analysis showed that $\sim 97\text{--}98\%$ of the total population of grains consists of monocrystalline and subrounded grains, i.e., ranging from subangular to rounded. The majority of these monocrystalline grains ($\sim 60\text{--}70\%$ of the total population) contain intersecting patterns of inclusion trails, inferred to originate from healed intragranular cracks. About 10% exhibit “closed,” more continuous intragranular cracks subparallel to the inclusion trails. Approximately 15% of the monocrystalline grains are characterized primarily by undulatory extinction. Less than 5% contain inclusion trails following the grain margin (i.e., “dust rims”) and/or “open” intragranular cracks. Less than 2–3% of the total population of grains is polycrystalline. These polycrystalline grains are subangular to subrounded and contain subgrains, randomly oriented inclusion trails, and short intragranular cracks.

Fractions of the sand, with grain sizes of 196 ± 16 , 275 ± 25 , and $378 \pm 22 \mu\text{m}$, were prepared by sieving (Figures 1b–1d). Analysis of images of the three fractions reported by Brzesowsky *et al.* [2011] showed that grain roundness, and hence the radius of curvature of grain asperities, increased with increasing grain size

2. Experimental Methods

We performed a total of 44 uniaxial, oedometer-type compaction experiments on loose sand aggregates, studying the effect of loading history, loading rate, grain size, initial porosity, and chemical environment on time-independent compaction behavior. An oedometer was used, rather than a hydrostatic compaction apparatus, as the former allows intrinsically better control and measurement of initial sample porosity before testing. Two series of experiments were performed:

1. Load-cycling experiments, performed on dry samples by cycling the applied (effective) stress from 0.24 MPa to a maximum of 30 MPa (equivalent to a burial depth or reservoir depth of 2.5–3 km) over a number of cycles. In all, 37 such tests were performed using three different grain-size batches ($196 \pm 16 \mu\text{m}$, $275 \pm 25 \mu\text{m}$, and $378 \pm 22 \mu\text{m}$), at loading rates of 3.9–390 MPa/h.

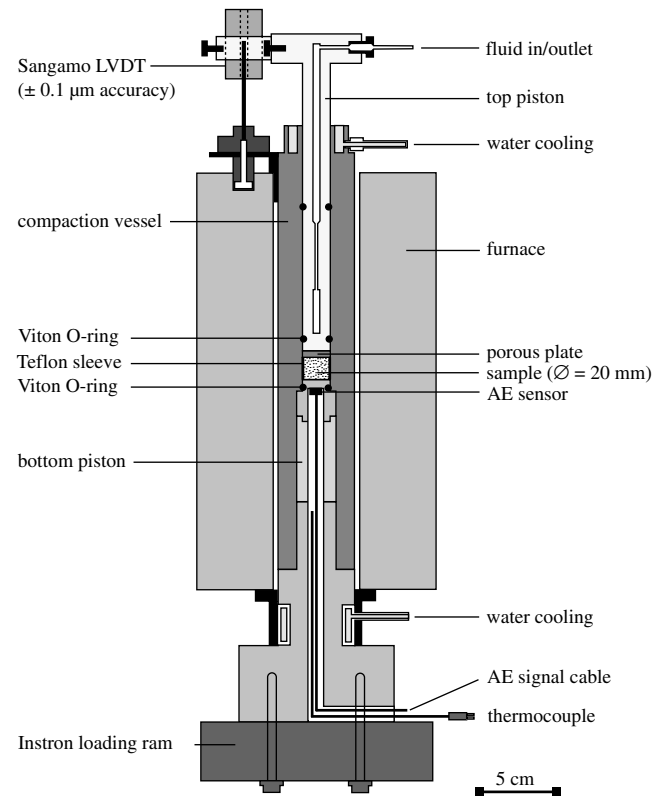


Figure 2. Semischematic diagram showing the uniaxial deformation apparatus or oedometer used in the present compaction experiments on sands.

[see Brzesowsky *et al.*, 2011, Figure 9]. This is in line with relationships known in sedimentary petrology and has been attributed to more effective abrasion of larger sized particles [Donaldson *et al.*, 1995].

Presaturated silica solution was prepared for use as a pore fluid by dissolving a fixed mass of sodium metasilicate ($\text{Na}_2\text{SiO}_3 \cdot 9\text{H}_2\text{O}$) in order to yield an equilibrium SiO_2 concentration of ~ 6 ppm at 25°C and 0.1 MPa fluid pressure [Hicks, 1989; Morey *et al.*, 1962; Rimstidt and Barnes, 1980; Robie *et al.*, 1978; Schutjens, 1991; Walther and Helgeson, 1977]. Subsequently, a small quantity of 0.1 M hydrochloric acid solution was added to obtain a pH between 6 and 7, resulting in a final composition of 6.3 ppm SiO_2 and $\sim 2 \cdot 10^{-4}$ M NaCl. Before use, silica saturation was attained by allowing the pore fluid to circulate in a closed polyfine container containing an excess of quartz sand. The use of saturated silica solution was adopted to minimize quartz dissolution by any mechanism other than stress-related solution transfer or corrosion effects. In addition, a small number of tests (two) were also performed using *n*-decane as pore fluid.

2.2. Experimental Setup and Acoustic Emission Monitoring

The compaction experiments were performed using an Instron 1362 servo-controlled testing machine, equipped with a 1-D (uniaxial) compaction vessel or oedometer (Figure 2). In this loading geometry, the sample undergoes uniaxial strain. The applied axial stress is the maximum principal stress σ_1 , while for loose granular samples [Karig and Hou, 1992] the lateral stresses ($\sigma_2 = \sigma_3$) are generally smaller than σ_1 , provided wall friction is low.

The vessel used in our experiments consists of a modified version of the oedometer described by Schutjens [1991] (see also Hangx *et al.* [2010]). The vessel and loading pistons are constructed from Monel K-500, a corrosion-resistant copper-nickel alloy, employed to minimize sample contamination by corrosion. The bottom piston is fixed within the vessel. The moveable top piston provides access to the pore fluid and is tipped with a porous plate, enabling evacuation of the sample and/or fluid introduction into the sample through the fluid in/outlet in the top piston. A Teflon ring behind the porous plate prevents sand grains from passing between the vessel wall and the top piston. Sealing of the top and bottom pistons is achieved using Viton O-rings, lubricated using Molykote 111 silicone grease.

Force applied to the top piston is measured externally using the Instron load cell (10 kN range, resolution ± 0.025 kN). Piston position and displacement are measured using both an LVDT (linear variable differential transformer, range ± 50 mm, resolution ± 2.5 μm) located in the Instron drive unit and a Sangamo LVDT (range ± 5 mm, resolution ± 0.1 μm) located between the upper piston and the vessel. Sample temperature is measured using a sheathed type-K (chromel/alumel) thermocouple (resolution 0.05°C) embedded in the vessel wall and electrically isolated with respect to the piston bore wall by a thin tube of Teflon (Figure 2).

In order to detect grain-scale brittle failure events, acoustic emissions can be counted using an acoustic emission (AE) monitoring system. The system used enables sensing, amplification, frequency filtering,

Table 1. Overview of Compaction Experiments Performed on Sands at Room Temperature

Experiment No.	Test Condition	Grain Size d (μm)	Loading Rate (MPa/h)	Cycling (C) or Direct Loading (DL)	Maximum Applied Stress σ_a (MPa)
Dry experiments (37 in total)					
BS1 to BS4	Lab-dry	275 ± 25	390	C	30
BS7, BS9	Evacuated	275 ± 25	390	C	30
BS8 ^a	Evacuated	275 ± 25	3.90	C	30
BS5, BS6, BS10 ^b , BS11 to BS13, BS30, BS31, BS44 ^c	Vacuum dried	275 ± 25	390	C	30
BS32	Vacuum dried	275 ± 25	390	C	22
BS24, BS25	Vacuum dried	196 ± 16	282	C	22
BS14 to BS23, BS29, BS33 to BS36	Vacuum dried	275 ± 25	282	C	22
BS26 to BS28	Vacuum dried	378 ± 22	282	C	22
Fluid-flooded experiments (7 in total)					
BS37, BS40, BS41	Aqueous solution ^d	275 ± 25	5495	DL	30
BS43	Aqueous solution ^d	275 ± 25	5495	DL	20
BS42	Aqueous solution ^d	275 ± 25	5495	DL	10
BS38, BS39	<i>n</i> -decane	275 ± 25	5495	DL	30

^aAfter load cycling, no subsequent creep stage was performed. The sample was removed from the vessel in a disturbed condition.

^bSample was tested in a Teflon pot, i.e., a Teflon sleeve closed at the bottom, and impregnated with resin prior to removal from the vessel.

^cSample was flooded with *n*-decane prior to removal from the vessel to enhance its cohesion.

^dThe aqueous solution consists of distilled water saturated with silica.

discrimination, and counting of wave packets emanating from microseismic events within the sample but not determination of AE energies. To detect AE emissions, an AE sensor (ceramic piezoelectric resonator) is located in the upper section of the bottom piston [Brzesowsky, 1995; Hangx *et al.*, 2010]. This is connected to a precision preamplifier (36 dB gain) and multistage signal conditioning system, the latter providing 24 dB gain and incorporating a 100 kHz to 1 MHz band-pass filter to eliminate low-frequency interference and sensor resonance effects. Events can be counted using two counter channels, for which a constant discrimination trigger threshold of 125 mV was set, just above noise level. Pulse stretching times (PST) for the two channels were set at 530 and 1000 μs , which served as a check for wave packet arrival-bunching effects and counter saturation. For well-spaced events, the count rates obtained by the two channels should be identical. The maximum effective AE event rate countable by the system was ~ 500 events per second.

2.3. Testing Procedure

Prior to each test, the vessel was fully assembled, except for the top piston. Tests were performed on individual sand samples (7.5 g in mass), taken from each of the three sieved fractions, under both dry and drained, fluid-flooded conditions, at ambient temperature and pressure. In setting up each experiment, the loose sand sample was first deposited into the open vessel using an elongated glass funnel to prevent grains from sticking to the vessel wall. In all cases, the vessel was lined with, and hence the sample was surrounded by, a thin-walled Teflon sleeve or pot (height 16 mm, thickness 0.13 ± 0.02 mm) previously inserted into the bore of the vessel to reduce friction between the sample and the vessel wall. After introduction of the sample, the top piston was inserted into the vessel until the sample was just touched, and the vessel was mounted into the Instron frame. The piston was then withdrawn by 1–2 mm and the vessel tapped with a mallet to let the sample settle and thus to obtain a near-constant sample length. The piston was then gently advanced in “position control” mode until a small “set point” load (0.075 kN; applied stress 0.24 MPa) was attained. At this stage, the system was switched into “load control” mode. The initial sample length (~ 16 mm) was then determined using the Instron LVDT as a measure of piston position and using a pair of vernier calipers (50 μm precision) to measure protrusion of the top piston from the vessel. The procedure produced a well-controlled starting aggregate with a reasonably reproducible porosity ϕ_i in the range 41–45%, with a mean and standard deviation of $42 \pm 0.3\%$ for all three batch sizes. We focused our experiments on samples in the latter range to investigate behavior at constant initial porosity but also tested a small number of samples outside this range (i.e., in the range 41–45%) for assessing the effects of varying ϕ_i . The initial agitation and minor loading of the sand was intended to produce a more or less locked aggregate aimed to diminish the role of pure interparticulate settling in accommodating compaction during loading. After determining their initial lengths, the sand samples were compacted under dry or fluid-flooded conditions, directly ramping or

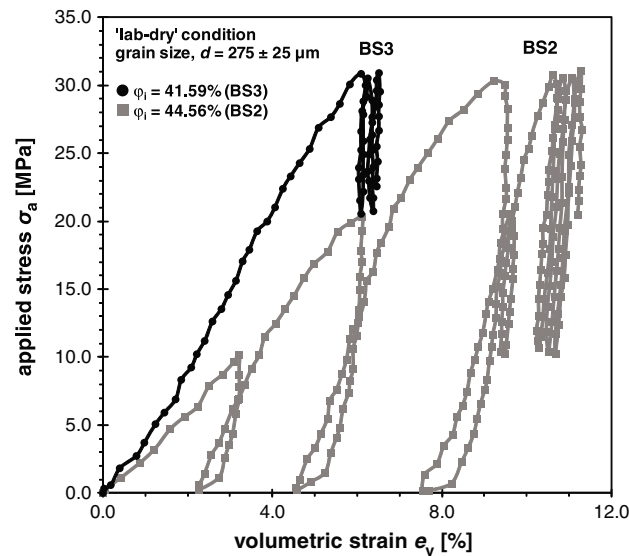


Figure 3. Typical applied stress versus volumetric strain plots, here representing compaction experiments BS2 and BS3, performed on sands of the $275 \pm 25 \mu\text{m}$ grain-size (d) fraction under lab-dry conditions (room temperature, loading rate = 390 MPa/h). The data illustrate that, with increasing initial porosity, more permanent deformation is obtained in loading cycles performed to successively higher stresses up to 30 MPa. Having reached 30 MPa, loading cycles at lower stresses exhibit quasi-elastic behavior.

cycling the applied stress σ_a in the range $0.24 \leq \sigma_a \leq 30$ MPa using constant loading rates of 3.90, 282, 390, and 5495 MPa/h. A summary of all 44 compaction experiments is shown in Table 1.

As mentioned above, the present tests were performed under dry conditions or flooded with an inert n -decane or silica-saturated solution under drained conditions (pore fluid pressure $P_p = 1$ atm). Three different “dry” states were investigated, referred to as the “lab-dry” (in equilibrium with lab air), “evacuated,” and “vacuum dried” conditions. The evacuated condition was achieved by simply attaching a vacuum hose line to the pore fluid in/outlet in the top piston (see Figure 2) after initial loading at 0.24 MPa, followed by evacuation using a single-stage rotary vacuum pump. This is assumed to have resulted in partial drying with respect to the lab-dry condition. For the vacuum dried tests, the vacuum pump was connected to the pore fluid inlet via a Drechsel bottle, which was filled with silicone oil, and then two glass

chambers, each filled with activated alumina serving as a drying agent (system vapor pressure: < 0.7 kPa). The latter was done to ensure that the vacuum dried system would be devoid of any water vapor. Drained, fluid-flooded test conditions were achieved by vacuum flooding the sample, at the initial set point load (0.24 MPa), either with n -decane (as-received analytical grade $\text{C}_{10}\text{H}_{22}$) or with the presaturated silica solution.

All tests were terminated by unloading the samples to the initial “set point” load (0.24 MPa) at a constant rate in the range 282–550 MPa/h. Fluid-flooded samples were then briefly evacuated to remove the bulk of the pore fluid phase (see Figure 2). After reducing the load fully to zero, the apparatus was taken out of the testing rig and dismantled in a vertical position, removing both the top piston and the lower segment of the bottom piston. Subsequently, while pressing a glass piston (external diameter = 20 mm) gently against the top of the sample to hold it in place, the vessel was turned upside down and the upper segment of the bottom piston was removed. Each sample was then carefully pressed out of the vessel, in an upward direction, into a glass tube (internal diameter = 20 mm) located in the position of the upper segment of the bottom piston. This allowed the sample, including the Teflon sleeve, to be recovered intact and placed in a cylindrical polyfine container. Fluid-flooded samples were then dried for 2–3 days at $\sim 70^\circ\text{C}$ in a drying oven. In this way, minimum disturbance to the friable sample structure was achieved. Prior to thin section preparation, samples were impregnated using a low-viscosity epoxy resin colored with a blue dye. Not all dry samples could be retrieved due to their loose nature. One sample (BS8) was removed dry, in disturbed condition. A second (BS10), tested using a Teflon pot (i.e., sleeve closed at bottom end), was impregnated with epoxy resin before removal from the vessel. A third (BS44) was flooded with n -decane upon return to the set point load to enhance its cohesion.

At the end of each sand compaction test, the Teflon sleeves or pot were found to be intact (i.e., not perforated by the sand grains) and of more or less unchanged thickness. Since the diameter of the vessel bore is 20 mm, the radius of the sample was taken as 9.9 mm when calculating the initial porosity at the set point load and the applied stress during the test. Note that porosity was calculated using the sample dimensions and samples mass, assuming a density for quartz of 2.648 g/cm^3 .

2.4. Data Acquisition and Processing

During the experiments, axial load, Instron LVDT position, Sangamo LVDT position, and temperature were logged at time intervals of 5, 10, or 300 s, depending on the applied loading rate. In addition, the cumulative

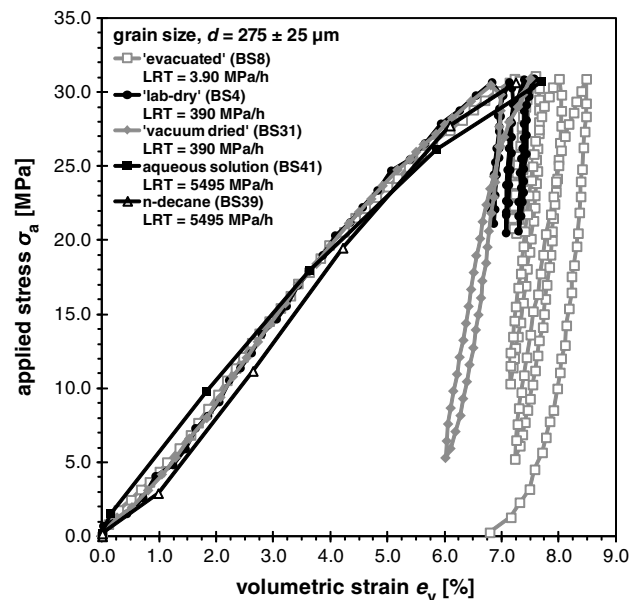


Figure 4. Applied stress versus volumetric strain data obtained from compaction experiments BS4, BS8, BS31, BS39, and BS41, performed on sands of the $275 \pm 25 \mu\text{m}$ grain-size (d) fraction under the various conditions shown and applying different constant loading rates (room temperature, initial porosity $\phi_i = 41.9 \pm 0.1\%$). The data show that there is no significant effect of loading rate or chemical environment on the compaction behavior.

number of acoustic emission events was logged by a separate system using the same time base. The Sangamo LVDT and raw Instron load and displacement data were used to construct volumetric strain versus applied axial stress plots. The displacement data were corrected for elastic distortion of the apparatus using predefined, tenth-order polynomial stiffness calibrations. Instantaneous volumetric strain was calculated directly from the displacement versus time records obtained for each experiment in terms of the engineering strain, defined as $e_v = -\frac{\Delta V}{V_0}$, which for our uniaxial compaction experiments is equal to $e_v = -\frac{\Delta L}{L_0}$. Conventional error analysis showed the absolute or relative errors in both logged and processed values of Instron load, Instron displacement, Sangamo LVDT displacement, applied axial stress, and volumetric strain to be less than 0.3%, 0.3%, 5 μm , 0.5%, and 0.6%, respectively. As these errors are smaller than the symbol size used in plotting our results, no attempt has been made to plot error bars

3. Experimental Results

Regardless of whether they were tested under dry or fluid-flooded conditions, all samples of the same grain size and initial porosity showed closely similar stress-strain behavior during load ramping and cycling. On the other hand, grain size and initial porosity significantly affected compaction behavior. We describe the trends observed below.

3.1. Mechanical Data

Typical applied stress versus volumetric strain plots reflecting the effect of loading history and initial porosity on the compaction of lab-dry sand from the $275 \pm 25 \mu\text{m}$ size fraction is depicted in Figure 3. Focusing on the cyclically loaded sample (BS2), this clearly illustrates our general observation that permanent deformation was always obtained in repeated loading cycles performed to successively higher stresses, in this case up to 30 MPa. Having achieved the maximum applied stress, repeated loading cycles between fixed limits at lower stresses produced reproducible, quasi-elastic (stable) hysteresis loops with diminishing or no further permanent deformation (BS2, Figure 3). In the quasi-elastic regions of these cycles, the average apparent constrained modulus was found to be $2.79 \pm 1.02 \text{ GPa}$. Comparing load-cycled sample BS2 ($\phi_i = 44.56\%$) with sample BS3 ($\phi_i = 41.59\%$), which underwent direct loading to 30 MPa, it is clear that more permanent deformation occurred in BS2 in reaching 30 MPa. This sample showed around 1.5 times more deformation than BS3 at 30 MPa and a total (tangent) compressibility around 1.38 times higher than BS3 during initial direct loading to 10 MPa (see Figure 3). The porosities attained by BS2 and BS3 at 30 MPa were 33.36 and 35.13%, respectively. Samples from the $275 \pm 25 \mu\text{m}$ grain-size fraction, with $\phi_i \geq 42 \pm 0.3\%$, attained a near-constant porosity of $37.4 \pm 0.3\%$ during initial loading up to 30 MPa.

A similar plot reflecting the effect of loading rate and chemical environment on samples from the $275 \pm 25 \mu\text{m}$ fraction, with $\phi_i = 41.9 \pm 0.1\%$, is shown in Figure 4. These experiments were conducted applying constant

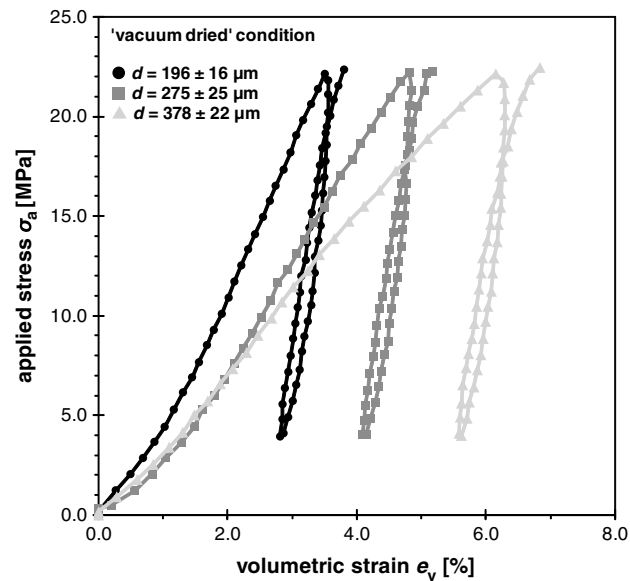


Figure 5. Applied stress versus volumetric strain plots obtained from compaction experiments BS19, BS25, and BS26, performed on sands of the 196 ± 16 , 275 ± 25 , and $378 \pm 22 \mu\text{m}$ grain-size fractions, under vacuum dried conditions (room temperature, initial porosity $\phi_i = 41.9 \pm 0.1\%$, loading rate = 282 MPa/h). The data demonstrate that with increasing grain size more permanent deformation is achieved.

progressive decrease in quasi-elastic stiffness with subsequent loading cycles reaching progressively lower stresses, with the average (apparent) constrained moduli of consecutive quasi-elastic loading cycles being 3.29 , 3.01 , and 2.48 GPa , respectively (Figure 4).

With regard to the influence of grain size, Figure 5 demonstrates a systematic effect of grain size on the stress-strain behavior for samples tested in the vacuum dried condition. Note that with increasing grain size more permanent deformation is achieved, i.e., the (finite, tangent) compressibility increases with increasing grain size. Cumulative AE event counts and AE rate, as well as the applied stress, obtained from a typical sand ($d = 275 \pm 25 \mu\text{m}$) loading test to 30 MPa , carried out in the vacuum dried condition, are plotted as a function of volumetric strain in Figure 6. These data (Figure 6) clearly illustrate that a larger cumulative AE event count is obtained at 30 MPa , when applying the short pulse stretching time (PST; $530 \mu\text{s}$) in comparison to the cumulative count acquired with the long PST ($1000 \mu\text{s}$). During unloading to 10 MPa and reloading to 30 MPa in a second cycle, AE emissions continue but to a reduced extent, though evolving similarly with strain during the reloading stage as during initial loading.

3.2. Microstructural Analysis

Thin sections of the deformed and impregnated sand samples were prepared from perpendicular slices cut parallel to the sample axis. These were analyzed using transmission optical microscopy. We focus on describing the microstructures developed in dry-tested samples deformed (load cycled) to maximum applied stresses of 30 MPa (BS8, BS10, and BS44) and 22 MPa (BS14). Of these samples, BS10 and BS44 suffered minor creep deformation after final load ramping to the maximum stress applied. However, the strains accumulated during creep were so small ($< 1\%$), compared with the strain accumulated beforehand ($\sim 7\%$), that any effects on microstructure would be insignificant and can be safely neglected.

From the outset, we note that no obvious unloading features (horizontal cracks) or compaction band features were apparent in the samples. In our analysis, crack density (defined here as the mean number of cracks per grain) and the fraction of failed grains F_{bg} were obtained by point-counting of over 500 grains, using the line interception method applied to representative thin sections. All compacted samples showed evidence of intragranular and transgranular cracking of grains, seen as cone cracks occurring within grains (intragranular cracks) and crosscutting grains (transgranular cracks), fanning out from grain-to-grain contacts.

loading rates of 3.90 , 390 , and 5495 MPa/h , corresponding to strain rates in the range 10^{-6} to 10^{-3} s^{-1} . With reference to Figure 4, the slowest loading test was carried out in the evacuated condition, while the tests at the intermediate loading rate were done under lab-dry and vacuum dried conditions. The fastest loading tests were performed under drained conditions using *n*-decane or silica-saturated water as pore fluid. The data presented in Figure 4 are typical of our results for fixed grain size and starting porosity and show no significant effect of either loading rate or chemical environment. This is evident from the fact that the stress-strain curves obtained from the tests under dry conditions (lab-dry, evacuated, and vacuum dried) correspond to those obtained from drained tests conducted using an inert pore fluid. Similarly, the behavior shown by samples flooded with *n*-decane is much like that of sands tested with silica solution as pore fluid. The stress-strain data obtained for the slowest (evacuated) loading test exhibit a

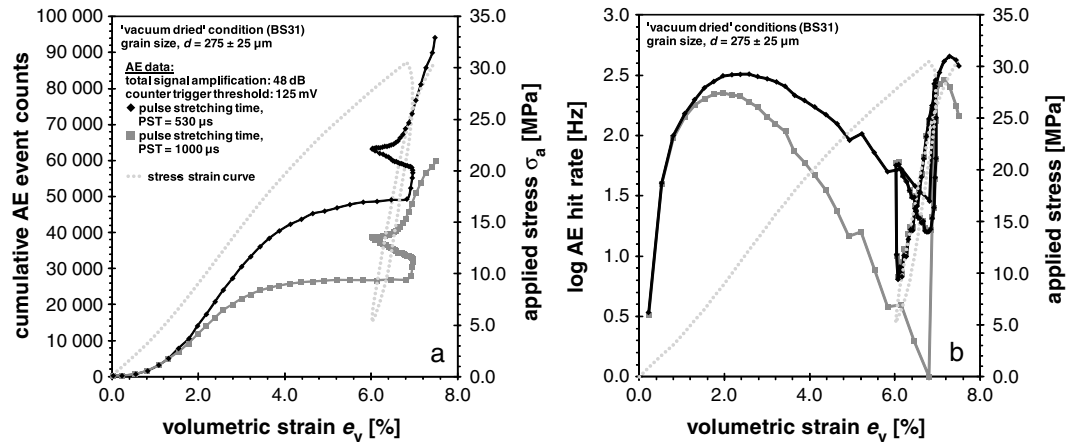


Figure 6. (a) Cumulative AE event counts and applied stress obtained during a typical compaction test (BS31) performed on sands of the $275 \pm 25 \mu\text{m}$ grain-size fraction under vacuum dried conditions (room temperature, loading rate = 390 MPa/h). The data clearly illustrate that a larger cumulative AE count is obtained when applying the shorter pulse stretching time. (b) Plot of AE event count rate and applied stress versus volumetric strain (e_v) constructed from Figure 6a. Note that both the cumulative AE event counts and the AE event count rate data diverge and flatten off after reaching the inflection point in the stress-strain curve ($\sigma_a > 5 \text{ MPa}$; 100–400 Hz). Beyond an applied stress of $\sim 10 \text{ MPa}$, the AE event count rate decreases again.

In samples cycled to a maximum stress of 30 MPa (samples BS8, BS10, and BS44), $\sim 30\%$ of the sand grains exhibit signs of failure (Figure 7a). Microcracks cut the preexisting closed cracks and the inclusion trails observed in the undeformed sands (Figure 7b) but do not widen/grow to such an extent that the grains loose cohesion. In sample BS8, which was physically disturbed during handling after deformation, disaggregated grains showed a major size reduction and a high angularity. In samples retrieved undisturbed (BS10 and BS44), cracks fan out from crushed, grain-to-grain contacts (Figure 7b). These brittle deformation features appear to be homogeneously distributed throughout the samples, with no signs of failure localization or of clustering or linkage of failed grains (Figure 7a). Furthermore, neither the transgranular nor intragranular cracks show any preferred orientation, resulting in an essentially random crack pattern. The fraction of broken grains F_{bg} was point counted in samples BS10 and BS44, which were cycled up to 30 MPa, yielding values of

36% and 38%, observing 591 and 751 grains, respectively. At lower applied stress (BS14; $\sigma_a = 22 \text{ MPa}$), similar deformation features are seen, although the amount of microstructural damage accumulated is significantly lower (Figure 7c).

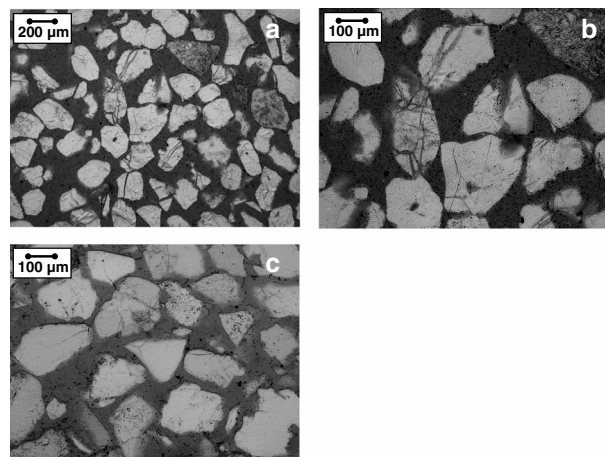


Figure 7. Optical micrographs of samples compacted under vacuum dried conditions at room temperature. Compaction direction is vertical. (a) Overview of the microstructure observed in sample BS44 ($\sigma_a = 30 \text{ MPa}$, $d = 275 \pm 25 \mu\text{m}$), showing that $\sim 30\%$ of the grains are broken. (b) Detail of Figure 7a displaying cracks fanning out from crushed grain contacts. As can be seen, some of the cracks cut through the preexisting closed cracks and inclusion trails. (c) Overview of the microstructure observed in sample BS14 ($\sigma_a = 22 \text{ MPa}$, $d = 275 \pm 25 \mu\text{m}$). Note that the failure features are similar, though the accumulated amount of damage is lower.

4. Interpretation of Experimental Results

From the mechanical and AE data presented in Figures 3 to 6, it can be concluded that after initial loading to stresses up to 30 MPa, dry load-cycling behavior at lower stresses is quasi-elastic and, therefore, presumably does not change the microstructure greatly, despite some ongoing AE activity. The observed quasi-elastic cycling and AE behavior also demonstrate that initial loading is accompanied by a large amount of irreversible, inelastic deformation, presumably involving grain fracturing or contact crushing and intergranular

sliding, rotation, and rearrangement. The same presumably goes for fluid-flooded samples, as these show closely similar loading behavior.

Focusing on the dry-tested samples from the $275 \pm 25 \mu\text{m}$ batch, the larger permanent deformation attained during (initial) loading of samples having larger initial porosities φ_i (i.e., comparing BS3 and BS2 in Figure 3, with those with $\varphi_i = 41.9 \pm 0.1\%$ in Figure 4) demonstrates a high sensitivity of compaction and (tangent) compressibility to φ_i . This could be an effect of early grain rearrangement or settling with relatively little breakage, occurring in the more porous samples en route to an aggregate state characteristic of the lowest initial porosities. However, it could also reflect enhanced intergranular stresses and hence increased contact distortion, grain failure, and associated rearrangement throughout the full loading history, when φ_i is high.

The absence of a clear effect of loading rate on our samples, within the range investigated, suggests that time-dependent compaction mechanisms play no significant role on the timescales of the load ramping and load-cycling sequences employed in the present tests, i.e., at strain rates of 10^{-6} to 10^{-3} s^{-1} . Likewise, the insignificant effect of chemical environment, specifically the various dry states employed versus flooding with *n*-decane as an inert pore fluid, indicates that purely frictional compaction mechanisms, such as intergranular sliding and rotation, play a minor role even at the fastest loading rate. Finally, adding a chemically active aqueous fluid did not enhance compaction, implying that water does not significantly promote deformation at the timescale investigated, either via equilibrium crack extension plus grain failure or via crack growth by stress corrosion plus grain failure or by any other mechanism (see also *Hangx et al.* [2010]).

From the microstructural observations made on samples tested under evacuated and vacuum dried conditions (BS8, BS10, and BS44; Table 1 and Figure 4), compaction of all samples is inferred to have involved particle crushing caused by transgranular and intragranular cracking. Since loading cycles conducted after attaining the maximum applied stress of 30 MPa are reproducible, and since relatively little permanent deformation occurred after initial loading to 30 MPa, presumably the microstructure does not change much beyond this point. On this basis the fraction of broken grains (F_{bg}) determined from thin sections of these samples (BS8, BS10, and BS44) is thought to represent an upper bound estimate of F_{bg} for the corresponding maximum stress level (30 MPa) and grain size of $275 \pm 25 \mu\text{m}$.

The AE events observed during sand compaction are inferred to be caused by grain crushing involving transgranular or intragranular cracking and by sliding-induced rearrangement of grains and grain fragments. The cumulative AE event counts depicted in Figure 6a were used to construct plots of AE event count rate (average rate for a particular time interval) and applied stress σ_a versus volumetric strain displayed in Figure 6b. It can be seen that up to the inflection point in the stress-strain curve, produced during initial loading, AE cumulative counts and count rate increases. Beyond this point, both the cumulative counts and count rates flatten off, with the count rates decreasing at applied stresses of > 10 MPa. Upon unloading, a rapid, short-lived increase in AE counts and count rate is seen, followed by a decrease in both with further unloading. Upon reloading, similar AE versus stress behavior is observed as during initial loading but now achieved in smaller elastic strains. This suggests no essential change in AE type between loading and reloading. Furthermore, the AE event count rates recorded by the counters with different pulse stretching time (PST) diverge above 5 MPa. The leveling off illustrates the inability of the AE signal conditioning system to count AE events at event rates above 500 Hz. The divergence and the leveling off reflect the effect of the different PSTs for the two counting channels. It is widely accepted that undercounting of AE events, known as the masking effect, will occur due to (i) the distributed nature of the occurrence (interval) time of AE events in relation to the PST applied, (ii) the amplitude distribution of AE events resulting in an underestimate of the number of small amplitude events, if these are concealed by overlapping large-amplitude, i.e., long-duration, events, and (iii) attenuation of AE waveforms to levels below discrimination [*Cox and Meredith*, 1993; *Lockner*, 1993; *Oda et al.*, 1989]. In addition, the time interval between consecutive AE events (the occurrence time) is generally considered as a purely random, noninteractive discrete point process, following, e.g., a Poisson distribution [*Lockner*, 1993; *Nishizawa and Noro*, 1990; *Oda et al.*, 1989]. However, it is plausible that during the sand loading experiments, grain failure interaction effects will occur, giving rise to clustering of AE events in space and time and hence causing additional undercounting of AE events due to an enhancement of the effect described under (i). Consequently, the AE event count rate data for both PSTs shown in Figure 6b, at values of the applied stress above 5 MPa, should be regarded an underestimate of the actual AE event rate.

Nonetheless, the AE data do serve to indicate that brittle events were important during the present experiments, with AE event count rates exceeding 500 per second at stresses around 10 MPa.

In conclusion, integrating the interpretation of the mechanical, microstructural, and AE data discussed above, compaction of the present sand aggregates is inferred to be primarily controlled by elastic distortion and grain crushing, coupled with grain rotation/sliding and rearrangement, and to be favored at larger grain sizes and in samples with larger initial porosity.

5. Microphysical Model for Sand Compaction by Hertzian Distortion and Grain Crushing

On the basis of the experimental results presented in this paper, a microphysical model for time-independent compaction of sands is now developed. In line with the conclusions drawn from the mechanical, microstructural, and AE data, sand aggregate compaction during loading is modeled as the sum of (1) elastic strain due to Hertzian grain contact distortion and (2) inelastic strain due to crushing (instantaneous failure) of individual grains or grain contacts, the latter contributing an incremental volume change due to subsequent, sliding-induced rearrangement of grains and grain fragments. The sand aggregate is treated as a simple cubic pack of same-sized grains, i.e., a pack of nominally spherical grains sited at the corners of a cubic unit cell with edge dimensions equal to the grain diameter. The simple cubic pack is characterized by a coordination number (c.n.) of 6 and by a porosity of 47.64% for perfectly spherical grains. It was chosen because real aggregates of same-sized particles are known to be characterized by a similarly low coordination number [Guimaraes *et al.*, 2007; McDowell and Bolton, 1998]. Other key assumptions are that no interaction occurs between grain failure events and that, after grain failure and subsequent rearrangement, the spatial structure of the aggregate can still be approximated by the ordered packing initially assumed. Note that on the basis of percolation theory [Isichenko, 1992; Stauffer and Aharony, 1992; Zallen, 1983], large-scale interactions are not expected below a threshold of 32% of the grains having failed for a simple cubic pack. A further assumption is that the grains and/or grain contact regions can be treated as Hertzian solids of revolution, i.e., torsionless axisymmetric loading is assumed to occur at each contact, over a frictionless circular planar contact area with radius a [Brzesowsky, 1995]. In addition, the remote state of applied stress (σ_a) is regarded as hydrostatic, and the grain contact force distribution is assumed uniform. These last two assumptions are justified as follows. First, the ratio of the axial stress to radial stress for the present 1-D compaction experiments is probably close to 1, as demonstrated in previous oedometric studies of similar materials [Chang *et al.*, 1992; Chang, 1993; Karig and Hou, 1992; Lambe and Whitman, 1979]. Thus, in accordance with the assumption of frictionless grain contacts, and the steps taken to minimize vessel wall friction in our experiments, considering the applied uniaxial stress to be homogeneously and isotropically transmitted throughout the sample is a reasonable first approximation. Second, deformation features were found to be uniformly distributed (no localization occurs) and cracks randomly oriented in our deformed samples, suggesting that grain contact disorder and collective restructuring of grain arrays are unimportant.

5.1. Grain Contact Force and Properties of an Ordered Pack

The first step in developing the present model is to specify the magnitude of the grain contact force in an ordered pack, as well as some basic relations defining pack volume and porosity. According to Hertzian theory, the total normal load F exerted between two grains across a contact can be written as [Huber, 1904]

$$F = \frac{2\pi\sigma_0 a^2}{3} \tag{1}$$

where σ_0 is the normal stress at the center of the contact. The radius a of the contact circle between two grains is described by the relation $a^3 = 3FR_r/(4E^*)$, where R_r is the relative radius of curvature defined as $1/R_r = (1/R_1) + (1/R_2)$ and $1/E^* = (1 - \nu_1^2)/E_1 + (1 - \nu_2^2)/E_2$ with R_i , ν_i and E_i ($i = 1, 2$) being respectively the radii of curvature (of the spherical unloaded grain contact surfaces), the Poisson's ratios and the Young's moduli of the two grains. Alternatively, F can be expressed as $\pi a^2 \sigma_n$ where σ_n is the mean normal contact stress. In any ordered pack of grains of diameter d , the force balance condition prescribes the applied stress σ_a to be equal to $\zeta \pi a^2 \sigma_n / d^2$. The scaling factor ζ is 1 for a simple cubic (SC) pack (c.n. = 6) of spherical grains. For comparison, in a simple hexagonal (SH) pack (c.n. = 8, porosity 39.54%) ζ is $2/\sqrt{3}$, while for face centered cubic (FCC) packing (c.n. = 12, porosity = 26.0%) it is $2/\sqrt{2}$. For readers not familiar with these geometries, a simple hexagonal

pack can be described in terms of a unit cell composed of two layers of vertically stacked spheres, with the spheres in each layer being located at the center and vertices of a hexagon. In an FCC pack, the constituent spheres are sited at the corners and at the face centers of a cubic unit cell with edge dimensions equal to $\sqrt{2}d$.

For any regular packing geometry, the initial (external) volume V_0 of a sand aggregate with mass m_a and solid phase density ρ_m is given as

$$V_0 = \eta N_0 d^3 = \eta \left(\frac{6m_a}{\pi \rho_m d^3} \right) d^3 = \frac{6\eta m_a}{\pi \rho_m} \quad (2)$$

where N_0 is the number of intact grains in the starting pack and the product ηd^3 represents the corresponding unit cell volume per grain. From this, it is easily shown that the initial aggregate porosity (ϕ_i) can be expressed as $1 - (\pi/6\eta)$. The scaling factor η ranges from 1 for SC packing ($\phi_i = 47.6\%$), to $\frac{1}{2}\sqrt{3}$ for SH packing ($\phi_i = 39.5\%$), and to $\frac{1}{2}\sqrt{2}$ for FCC packing ($\phi_i = 26.0\%$).

5.2. Contact Force Enhancement During Compaction

After failure and local rearrangement, a grain in the aggregate spatial structure can be envisaged (i) to remain near-intact and hence load supporting, (ii) to be replaced by many small fragments, such that repacking equivalent to removing the original grain occurs without changing the load supported by the surrounding grains, or (iii) to remain near-intact but to no longer support load and hence to increase the load on surrounding grains without significantly changing the previously assumed packing structure. For situations (i) and (ii), the grain contact normal load F remains as given in equation (1). For situation (iii), load enhancement at a given applied stress σ_a can be incorporated following the relation

$$F = \frac{\sigma_a d^2}{\zeta} \frac{N_0}{N_0 - n_N} \quad (3)$$

where n_N is the cumulative number of failed grains at any instant during loading. In the present model, we investigate these two end-member cases of grain loading after grain failure, using equation (1) or (3), instead of attempting to scale contact forces to account for reduction of grain size by failure. We choose this route as we have no way of quantifying the size and strength behavior of grains that have failed already.

5.3. Grain Failure Criterion

Having considered the magnitude of the force transmitted across grain contacts in the model pack, grain crushing is now accounted for by applying the grain failure criterion, based on the Hertzian/LEFM model for the crushing of individual sand grains, developed by Brzesowsky *et al.* [2011]. We assume that impinging grains can be envisaged as elastic solids in idealized Hertzian elastic contact, with Griffith-type surface flaws of initial dimension c_0 being present over all grain surfaces before loading. In addition, we assume that flaws aligned tangentially to the periphery of the circular grain contacts (i.e., flaws aligned subnormal to the plane of grain contact) can be considered to be edge cracks subjected to the maximum tensile radial stress $\sigma_T = (1 - 2\nu)\sigma_0/3$ predicted by the Hertz analysis [Huber, 1904], so that the crack tip stress is characterized by the mode I stress intensity factor $K_I = Y\sigma_T\sqrt{\pi c}$. Such a flaw is viewed to evolve into an extensional ring crack at the edge of the contact and to initiate grain failure when σ_T exceeds the cohesive tensile strength of the grain material or, in terms of LEFM, when K_I attains a critical level equal to the fracture toughness $K_{c,I}$, i.e., if $K_I = Y\sigma_T\sqrt{\pi c} \rightarrow K_{c,I}$. In general, the possibility of both equilibrium and subcritical extension of the initial Griffith flaw would mean that the critical flaw size $c_f \geq c_0$. It is assumed that a crack of dimension c_f will remain unstable along its advancement path, causing instantaneous/catastrophic grain failure.

Making use of the relations for σ_T , σ_0 , a , and $K_I = K_{c,I}$ given above, the critical contact force at failure (F_c) for an individual grain is now given by the criterion

$$F_c = \frac{9\pi\sqrt{\pi}K_{c,I}^3 R_f^2}{2c_f\sqrt{c_f}Y^3(1-2\nu)^3(E^*)^2} \quad (4)$$

If all grains in the model pack were identical and contained identical surface flaws (or flaws at failure), the above would predict simultaneous failure of all grains at a fixed applied stress. This is clearly unrealistic. In reality, F_c will be a distributed quantity due to the distributed nature of c_f and R_f at the grain-to-grain level

(see also *Brzesowsky et al.* [2011]). Bearing this in mind, the model can be extended to a population of grains having distributed F_c by considering two extreme cases: (I) spherical grains with constant radius of curvature R ($R = d/2$, so $R_r = d/4$) plus a grain-to-grain distribution of flaw sizes at failure c_f (assumed constant per grain), with the failure criterion expressible in terms of F as

$$(c_f)_c = \left(\frac{K_{c,I}}{Y\sigma_T\sqrt{\pi}} \right)^2 = 4\pi \left(\frac{K_{c,I}a^2}{Y(1-2\nu)F} \right)^2 = 3\pi \left(\frac{K_{c,I}}{Y(1-2\nu)} \right)^2 \sqrt{\frac{3}{4F^2} \left(\frac{R_r}{E^*} \right)^4} \quad (5)$$

or (II) nonspherical grains with constant flaw size at failure c_f , plus a grain-to-grain distribution of effective radius of curvature r_g , characterizing distributed contact asperity amplitude, with the fracture criterion expressible in terms of F as

$$(r_g)_c = \frac{4RE^*a^3}{3RF - 4E^*a^3} = \left(\left(\frac{3}{2F} \right) \sqrt{\frac{1}{2F} \left(\frac{K_{c,I}}{Y(1-2\nu)} \right)^3 \frac{\pi\sqrt{\pi}}{c_f\sqrt{c_f}} - 1} \right)^{-1} \quad (6)$$

Implicit in case (II) of the model is the assumption that, despite the nonspherical nature of the grains, the aggregate spatial structure can be treated as an ordered packing with an equivalent-sphere mean grain size d_{eq} . Furthermore, an asperity with effective radius of curvature r_g , on a specific grain, is considered to be always in contact with that side of a neighboring grain whose radius of curvature R ($\neq r_g$) is described by the relation $d_{eq} = 2R$. Accordingly, R_r is expressed as $r_gR/(r_g + R) = r_gd_{eq}/(2r_g + d_{eq})$.

5.4. Inelastic Strain

Grain failure is considered to contribute to an incremental volume change equal to αd^3 or αd_{eq}^3 , where α is a dimensionless constant ($0 \leq \alpha \leq \pi/6$) and d_{eq} is the equivalent-sphere mean grain size calculated from the average grain mass. At a given applied load, a cumulative number n_N of grains will have failed contributing an inelastic volumetric strain $e_v^{inel} = (n_N \alpha d_{eq}^3)/V_0 = (\alpha/\eta)(n_N/N_0)$. Now, the ratio n_N/N_0 ($\lim N_0 \rightarrow \infty$) represents the cumulative probability of grain failure at a load $F \leq F_c$, i.e., $P_r[F \leq F_c]$, and is therefore expressible using any suitable cumulative distribution function. Furthermore, it follows from equations (4) to (6) that the probability $P_r[F \leq F_c]$ coincides with the probability of existence of a grain with a flaw at failure of size $c \geq (c_f)_c$ or an effective radius of curvature of size $r_g \leq (r_g)_c$.

Assuming a Weibull distribution of c_f , the inelastic volumetric strain e_v^{inel} for case (I) of the model can accordingly be written as

$$e_{v(i)}^{inel} = \frac{\alpha n_N [c_f \geq (c_f)_c]}{\eta N_0} = \frac{\alpha}{\eta} (1 - W((c_f)_c)) = \frac{\alpha}{\eta} \exp \left[- \left(\frac{(c_f)_c}{k} \right)^m \right] \left(\lim_{N_0 \rightarrow \infty} \right) \quad (7)$$

where $n_N[c \geq (c_f)_c]$ is the cumulative number of (failed) grains with a flaw dimension at failure c_f greater than or equal to $(c_f)_c$ at a specific contact force F , and where $W((c_f)_c)$ is the Weibull cumulative distribution function, with k and m being the scale and shape parameters of this distribution [*Brzesowsky et al.*, 2011]. A Weibull distribution is chosen because both the density and the probability functions are convenient analytical functions passing through the origin.

Likewise, assuming a Weibull cumulative distribution of r_g , $W((r_g)_c)$, the inelastic volumetric strain for case (II) of the model can be expressed as

$$e_{v(ii)}^{inel} = \frac{\alpha n_N [r_g \leq (r_g)_c]}{\eta N_0} \approx \frac{\alpha}{\eta} W((r_g)_c) = \frac{\alpha}{\eta} \left(1 - \exp \left[- \left(\frac{(r_g)_c}{k} \right)^m \right] \right) \left(\lim_{N_0 \rightarrow \infty} \right) \quad (8)$$

where $n_N[r_g \leq (r_g)_c]$ is the cumulative number of (failed) grains with an effective radius of curvature r_g smaller than or equal to $(r_g)_c$ at contact force F .

5.5. Elastic Strain

Elastic strain is described along the lines of Hertzian contact distortion, defined as the mutual approach of grain centers during loading, following the relation $\delta = \pi a \sigma_o / (2E^*) = 3F / (4aE^*)$ [see *Johnson*, 1987, equation 4.20]. The linear elastic strain ε^{el} due to contact distortion of neighboring grains can be written as δ/d . Moreover, for any

ordered packing under a hydrostatic state of stress, the elastic volumetric strain e_v^{el} equals $1 - (1 - \epsilon_{el})^3$. For case (I) of the model, the linear elastic strain ϵ^{el} is accordingly given by

$$\epsilon_{(i)}^{el} = \frac{\delta}{d} = \frac{1}{d} \sqrt[3]{\frac{1}{R_r} \left(\frac{3F}{4E^*} \right)^2} \quad (9)$$

For case (II) of the model, the Hertzian distortion is distributed from grain contact to grain contact, through the distribution in r_g . The linear elastic strain ϵ^{el} can therefore be described as

$$\epsilon_{(ii)}^{el} = \frac{\delta_{tot}}{N_0 d_{eq}} \approx \sqrt[3]{\left(\frac{3F}{4d_{eq}^2 E^*} \right)^2} \int_0^\infty w((r_g)_c) \sqrt[3]{2 + \frac{d_{eq}}{(r_g)_c} d(r_g)_c} \left(\lim_{N_0 \rightarrow \infty} \right) \quad (10)$$

where δ_{tot} is the total elastic distortion considering N_0 contacting grains in a row and $w((r_g)_c)$ is the probability density function of the assumed Weibull distribution of r_g .

5.6. Final Model

Our final expression for total volumetric strain e_v^{tot} as a function of σ_a is obtained adopting the relation $e_v^{tot} = e_v^{inel} + e_v^{el}$. For case (I) of the model, substitution of equation (3) and the relation $R_r = d/4$ into equations (5) and (9) demonstrates $(c_f)_c$ and the elastic strain to be grain-size independent. The inelastic strain for case (I) of the model only exhibits grain-size dependence if the Weibull parameters m and k are grain-size dependent. For case (II) of the model, substitution of equation (3) and the relation $2R = d_{eq}$ into equations (6) and (10) illustrates $(r_g)_c$ and the elastic strain to be grain-size dependent, the latter dependence being due only to the definite integral involved.

Brzesowsky et al. [2011] discussed how the Weibull weakest link theory [*Weibull*, 1951] can be used to directly express the failure probability of a material, such as an aggregate, in terms of the failure probability of its elemental volumes, i.e., the constituent grains. In that framework, each grain is considered to possess a distributed failure stress or strength (σ_T). In contrast, the present approach associates each grain with a specific σ_T which can essentially be interpreted as the mean value of an extremely narrow strength distribution per grain. Consequently, the distributed nature of σ_T through the aggregate, considered in the present analysis, represents a distribution of mean grain strengths. It should be noted, however, that contrary to the Weibull weakest link concept, the present model envisages that elemental grain failure causes only an increment of inelastic volumetric strain rather than global material failure.

6. Comparison of Experimental Results With Microphysical Model Simulations

In order to compare our experimental data on sand compaction (cf. section 3.1) with the compaction behavior predicted by the above microphysical model, the model has been used as a basis for numerical simulations focusing on the effect of grain size (d or d_{eq}). We have also conducted runs to investigate the sensitivity of our results to initial porosity (ϕ_i), packing structure (SC versus SH), the factor α , and the Weibull parameters m and k .

6.1. Choice of Numerical Values

Applied stress σ_a versus total volumetric strain e_v^{tot} data have been computed employing the model for both extreme cases (I and II) and increasing the applied load in equally spaced steps of 0.01 N (or 0.05 N) to obtain σ_a data up to 22 MPa. This applied stress was chosen to represent experiments BS19, BS25, and BS26, performed under the same conditions, but for different grain sizes (respectively, 275, 196, and 378 μm). For the purpose of simulating subsequent unloading to 3.5 MPa, similar σ_a - e_v^{tot} data sets were computed considering only the elastic recovery of the aggregate. Load cycling was not simulated since no allowances were made for any hysteresis effects in the model. For case (I) of the model, the grain size d was taken equal to 196, 275, or 378 μm , corresponding to the mean grain sizes of the above mentioned samples and thus of all sieved fractions used in this study. For case (II) of the model, d_{eq} was chosen equal to 208, 279, or 399 μm , corresponding to the equivalent-sphere mean grain size (d_{eq}) calculated for each grain-size fraction.

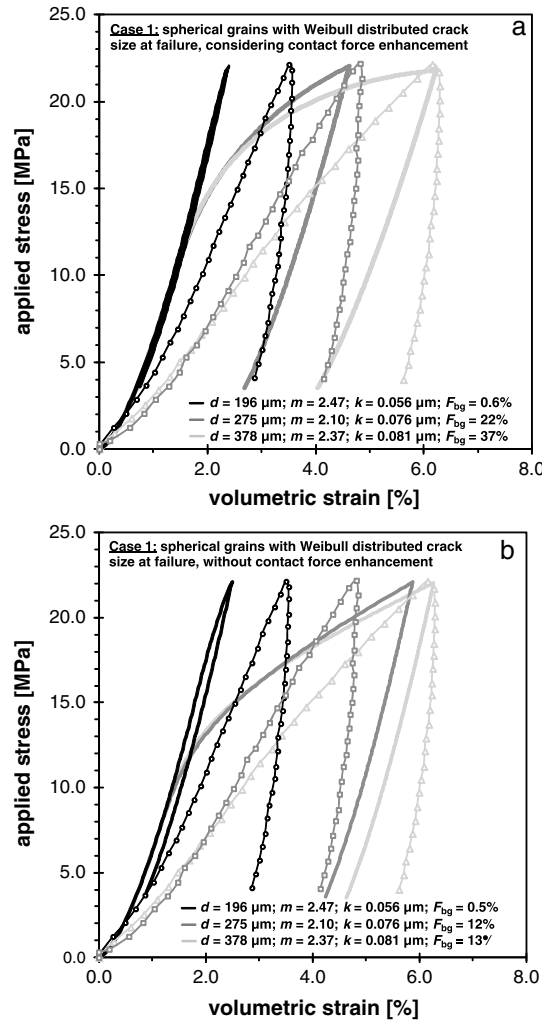


Figure 8. Applied stress versus volumetric strain curves computed from simulating case (I) of the microphysical model for sand compaction, namely, spherical grains with Weibull-distributed crack size at failure. (a) Simulations including contact force enhancement. The factor α fitted (0.085) falls well within its expected range. The fraction of broken grains (F_{bg}) computed at 22 MPa for a grain size of 378 μm is 37%. (b) Simulations with no contact force enhancement. In comparison to the results in Figure 8a, the fraction of broken grains at 22 MPa obtained for each grain size is substantially lower, while the factor α fitted (0.3) is acceptable. Note that the corresponding experimental data have been added for comparison (open symbols).

in the range $0 \leq \alpha \leq \pi/6$. In our individual reference simulations, the factor α was chosen such that the stress and the total volumetric strain (e_v^{tot}) at the point of load reversal exactly coincides with that point for the experimental data of the $378 \pm 22 \mu\text{m}$ fraction compacted under vacuum dried condition (sample BS26).

6.2. Simulation Results

The simulated σ_a - e_v^{tot} curves for our SC reference pack are depicted in Figures 8 and 9, together with the data obtained in experiments BS19, BS25, and BS26. Figure 8a shows σ_a - e_v^{tot} curves produced from simulating the microphysical model for case (I), namely, spherical grains with distributed crack size at failure (c_f), and considering contact force enhancement. The factor α fitted (0.085) falls well within its expected range of 0 to $\pi/6$.

Weibull parameters k and m characterizing the distribution of crack size at failure (c_f) or effective radius of curvature (r_g) of each grain-size batch were obtained from the crushing tests on single sand grains performed by Brzesowsky *et al.* [2011], using the same starting sand. This was done using the maximum likelihood estimation method [Johnson and Kotz, 1970], ignoring possible loading rate effects. Note that including the Weibull parameters k and m in this way introduces the grain-size dependence of c_f and r_g reported by Brzesowsky *et al.* into cases (I) and (II) of our model, respectively. For case (II) of the model, the Weibull parameters k and m were calculated taking c_f equal to 0.115 or 0.05 μm , i.e., the mean and, respectively, lower bound values of c_f obtained from the crushing tests performed by Brzesowsky *et al.* [2011] on visibly spherical single sand grains selected from the $378 \pm 22 \mu\text{m}$ grain-size batch.

The density, Young's modulus, and Poisson's ratio of quartz were taken as 2.648 g/cm^3 , 95.68 GPa, and 0.077, respectively [Simmons and Wang, 1971; Sumino and Anderson, 1984]. The elastic constants were computed on the basis of single crystal data applying the Hill averaging method, assuming a macroscopically homogeneous, isotropic polycrystalline aggregate of zero porosity, with random crystallographic orientation distributions [Birch, 1966]. This approach was used in order to take into account the random crystallographic orientation of sand grains in a stressed granular sample. The quartz fracture toughness (K_{Ic}) was taken as equal to $1 \text{ MN m}^{-3/2}$, a representative value based on double torsion tests on synthetic quartz single crystals at room temperature and under vacuum (0.1 Pa), ambient, or water-immersed conditions [Atkinson, 1979; Atkinson and Meredith, 1989; Darot and Gueguen, 1986; Gueguen *et al.*, 1990; Meredith and Atkinson, 1982; Reuschlé, 1989].

To serve as a reference case, a simple cubic (SC) packing was assumed, i.e., taking ζ and η equal to 1 and the initial porosity (ϕ_i) equal to 47.64%. As previously stated, the factor α should then lie

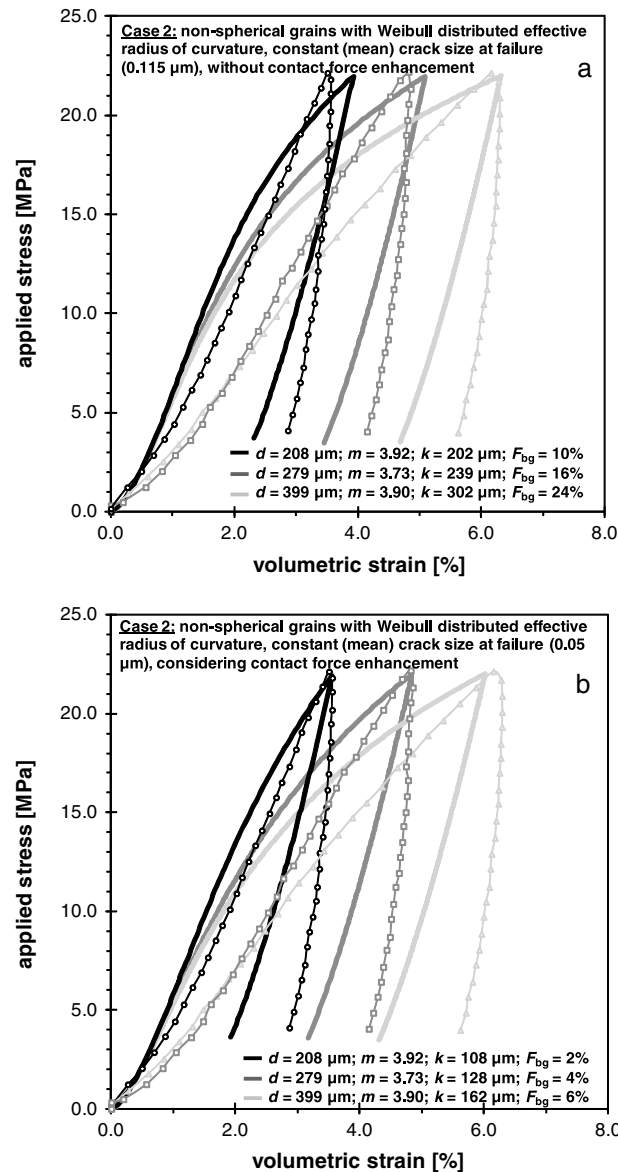


Figure 9. Applied stress versus volumetric strain curves computed from simulating case (II) of the microphysical model for sand compaction, namely, nonspherical grains with Weibull-distributed effective radius of curvature and a constant (mean) crack size c_f at failure. (a) Simulations taking c_f to be equal to 0.115 μm, including no contact force enhancement. The fraction of broken grains (F_{bg}) computed at 22 MPa for each grain size and the value of the factor α fitted are reasonable. (b) Simulations taking c_f to be equal to 0.05 μm and assuming contact force enhancement. Note that the fraction of broken grains computed at 22 MPa for each grain size is extremely low, yielding a fitted factor α of 0.57, which is slightly outside of its expected range. Note that the corresponding experimental data have been added for comparison (open symbols).

The F_{bg} value computed at 30 MPa for $d = 279 \mu\text{m}$ equals 12%.

Let us now focus on a comparison of our (SC) reference pack simulations with the experimental data (BS19, BS25, and BS26), as depicted in Figures 8 and 9. Both cases of the model predict $\sigma_a-e_v^{\text{tot}}$ curves for individual grain-size fractions that resemble the experimental data in form, as well as predicting the expected grain-size dependence, at least in terms of qualitative trend (increasing grain size promotes compaction). However,

However, the computed fraction of broken grains ($F_{bg} = n_N/N_0$, equations (7) and (8)) at 22 MPa for a grain size d of 378 μm (37%) is too large, i.e., greater than the threshold of 32% at which percolation theory implies interaction of grain failure events. The number of grain failure events (F_{bg}) predicted by our model is therefore inconsistent with our model assumption that there are no grain-scale interaction effects. For this reason, similar $\sigma_a-e_v^{\text{tot}}$ curves, depicted in Figure 8b, were constructed for case (I) of the model, disregarding load enhancement (i.e., without employing equation (3)), changing σ_a in steps of 0.22 MPa. In comparison to the results presented in Figure 8a, the F_{bg} values computed at 22 MPa are substantially lower. The fitted factor α in this case takes a value of 0.3, which is acceptable, and the F_{bg} value at 30 MPa equals 25% for $d = 275 \mu\text{m}$, which is also reasonable.

Figure 9a shows $\sigma_a-e_v^{\text{tot}}$ curves produced from simulating the microphysical model for case (II), namely, nonspherical grains with distributed effective radius of curvature (r_g) assuming constant (mean) c_f equal to 0.115 μm. Taking into account load enhancement, the F_{bg} values computed for each grain size became larger than 50% toward 15–20 MPa. For this reason, the $\sigma_a-e_v^{\text{tot}}$ curves depicted in Figure 9a were constructed without employing equation (3). The F_{bg} values obtained at 22 MPa and the fitted α value of 0.17 are reasonable. The F_{bg} value computed at 30 MPa for $d = 279 \mu\text{m}$ equals 49%. Similar $\sigma_a-e_v^{\text{tot}}$ curves, depicted in Figure 9b, were constructed for this case of the model assuming constant (lower bound) c_f equal to 0.05 μm, taking account load enhancement into account this time. The F_{bg} values obtained are extremely low, yielding a factor α equal to 0.57, which is too high in that it lies slightly outside the expected physically reasonable range. It should be noted, however, that the maximum α built into the model ($\pi/6$) could be larger if pore volume decrease due to grain failure is also considered.

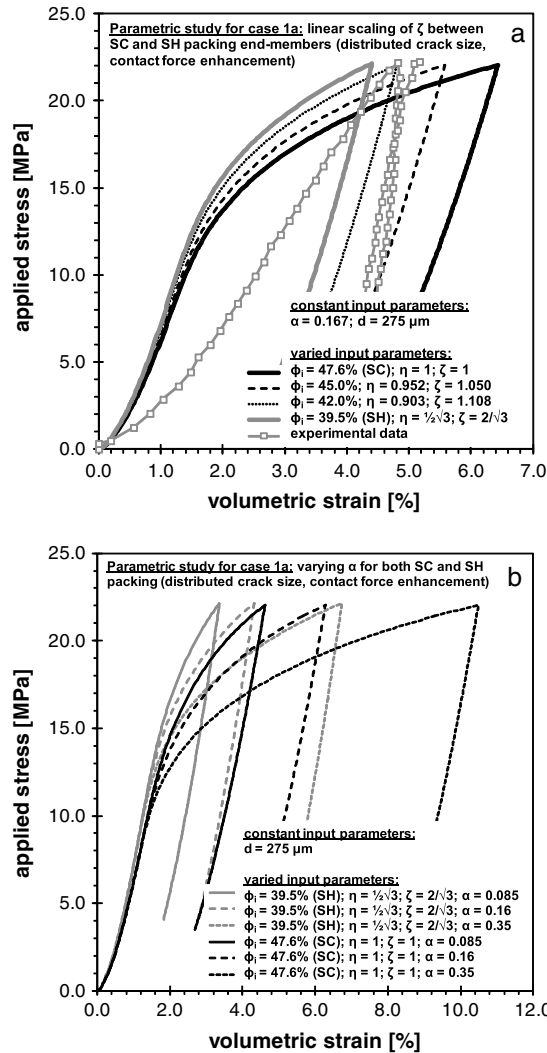


Figure 10. Parametric study for simulations from case (II) of the micro-physical model for sand compaction (spherical grains with Weibull-distributed crack size at failure, including contact force enhancement), showing computed applied stress versus volumetric strain curves. (a) Effect of the grain contact stress scaling factor ζ . The value of ζ is linearly interpolated between the value of $2/\sqrt{3}$ for an SH pack and 1 for an SC pack, according to chosen initial porosity values lying between the SH and SC values. (b) Effect of the amount of incremental volume change caused by failure of a single grain α . The value of α was varied from 0.085 to 0.16 to 0.35.

simulations, the inflection point reflects the influence of the Weibull distributions used. These distributions result in relatively few grain failure events at low strains, so that deformation is dominated by Hertzian elastic distortion at grain contacts, leading to increasing stiffness at low strains (i.e., concave up $\sigma_a-e_v^{\text{tot}}$ curves with relatively little influence of grain size; Figure 9b). At strains of around 1%, however, stresses become high enough to cause increasing amounts of grain failure as the peak of the relevant Weibull distribution is progressively accessed. This produces the predicted inflection point as the strain achieved per unit stress increase goes up, such that compressibility increases and the $\sigma_a-e_v^{\text{tot}}$ curves acquire a concave down form. This behavior seen in our model seems to offer a reasonable explanation for the form of the $\sigma_a-e_v^{\text{tot}}$ curves observed in our experiments (e.g., in Figure 9b). It should be noted, however, that such behavior will not be unique to a Weibull distribution and that the detailed shape of the predicted $\sigma_a-e_v^{\text{tot}}$ curves is for a large part determined by the chosen distribution and its parameters.

quantitative agreement between predicted and observed strains, at fixed stress levels, is poor especially at midrange stresses. Nonetheless, the $\sigma_a-e_v^{\text{tot}}$ curves, the grain-size dependence, and the fraction of broken grains at maximum σ_a for the simulation displayed in Figure 9b shows the best agreement with both the sand compaction test results (BS19, BS25, and BS26) and the fraction of broken grains estimated from thin sections of deformed material (cf. section 3.2). This simulation assumed (a) nonspherical grains with distributed effective grain radius of curvature, (b) constant c_f equal to $0.05 \mu\text{m}$, and (c) full load enhancement. On this basis, and taking into account the fact that the Weibull statistics describing the distribution of effective radius of curvature (r_g) are derived from failure data obtained on single sand grains from the same material [Brzesowsky *et al.*, 2011], we infer that the grain-size effect seen in the experimental data is not likely due to the grain-size-dependent departure from sphericity assumed in this case of the model. This hypothesis is supported by the argument presented by Brzesowsky *et al.* [2011] that there is no physical basis for a grain-size dependence of c_f whereas a grain-size dependence of surface sphericity radius is well known in sedimentology. In sedimentology, increasing asperity radius is believed to be related to more effective abrasion of larger sized grains during sand erosion and transport [Brzesowsky *et al.*, 2011; Donaldson *et al.*, 1995]. An additional argument that supports our inference regarding the observed grain-size effect is the experimental observation that aggregates of same-sized spherical glass beads show no systematic dependence of compaction strain on grain size under otherwise similar conditions (e.g., in the shear experiments reported by Anthony and Marone [2005]).

Regarding the shape of the predicted $\sigma_a-e_v^{\text{tot}}$ curves represented in Figure 9b (and indeed Figures 8 and 9a), we note that the characteristic inflection point seen in the experimental data is consistently reproduced for all grain sizes simulated. In our

Up to this point, we have used the simple cubic packing model (c.n. = 6, $\varphi_i = 47.64\%$) as a reference case for simulating grain aggregate compaction, thus capturing the low coordination number expected for same-sized grain-size batches of the type used in our experiments [Guimaraes *et al.*, 2007; McDowell and Bolton, 1998]. While the reference simulations represented in Figure 9b do offer an explanation for the observed form of the $\sigma_a - e_v^{\text{tot}}$ curves, the grain-size dependence and the fraction of broken grains attained at maximum σ_a , the initial porosity of the chosen packing is higher than in our experiments (47.64% versus a mean of $42.0 \pm 0.3\%$). Moreover, the chosen pack does not allow for the effect of initial porosity to be investigated or compared with the effect of initial porosity that is clearly visible in the experiments reported in Figure 3, where sample BS2 with $\varphi_i = 44.56\%$ showed 1.38 times more strain during initial loading than BS3 with $\varphi_i = 41.59\%$.

In order to address the effect of initial porosity on compaction behavior in our model, we explored the effect of varying φ_i between that for a SC pack (47.64%) and an SH pack (39.54%) by (1) linearly interpolating the value of the grain contact stress scaling factor ζ between the value of $2/\sqrt{3}$ for an SH pack and 1 for an SC pack, according to chosen initial porosity values lying between the SH and SC values, and (2) assuming that the contact stress scaling factor ζ stays equal to that for a SH pack but adjusting the initial aggregate porosity by removing a fixed number grains (n_R) from the SH pack to give the right φ_i . The latter method increases contact force in proportion to the reduced number of contacts in the same way that we already model contact force enhancement due to grains failure (see equation (3)). Porosity change in response to loading can further be changed by adjusting the value for α . Parameter α represents the linear scaling factor controlling the incremental volume change caused by failure of a single grain and will depend on φ_i to some extent, reflecting increased grain rearrangement. We accordingly investigated the sensitivity of stress-strain behavior to φ_i for $\alpha = 0.085, 0.16, \text{ and } 0.35$. The results obtained for both methods of exploring the effect of φ_i on compaction behavior are shown in Figure 10. The two methods yielded closely similar results and clearly demonstrate that increasing φ_i increases predicted aggregate compressibility. Though the magnitude of the effect is somewhat lower (about half), the results do show a similar order of sensitivity of sample compressibility to φ_i to that observed in our experiments (e.g., BS2 versus BS3, Figure 3). This supports our earlier interpretation that higher porosities imply higher contact stresses (modeled), which cause increased elastic distortion and grain failure, coupled with enhanced grain rotation/sliding and rearrangement (not explicitly modeled).

At the same time, however, the modeling results exemplified by Figure 10 also show that the experimentally observed dependence of “compressibility” on φ_i , or indeed the detailed shape of the $\sigma_a - e_v^{\text{tot}}$ curves obtained in any individual experiment, cannot solely be explained in terms of combined effects of changing contact forces and varying α , unless perhaps α is characterized by higher values during initial loading due to a repacking effect, especially in higher porosity aggregates. To assess whether better agreement can be obtained between our model, as applied for case (II) (nonspherical grains with distributed effective radius of curvature, r_g), and the experimental data as presented in Figure 9b, we have varied not only α and φ_i but also the parameters k and m in the Weibull function representing the distribution of c_f and r_g . As already mentioned, k and m also influence the shape of the predicted stress-strain curves, potentially making them too steep during initial loading and too rounded or shallow toward the final volumetric strain. By varying k , m , and α , in reasonable ranges for specific initial porosities, better agreement can be obtained between our simulations and our experimental results than obtained in Figures 9 and 10, for example. However, given (a) the constraints that we have on k and m from the measurements on single grains reported by Brzesowsky *et al.* [2011], (b) the fact that the type of distribution function used in modeling influences the detailed shape of predicted stress-strain curves, and (c) the absence of independent constraints on α and its likely dependence on porosity, little significance can be attached to better fits obtained by adjusting all these parameters. For this reason, we do not report the results of these fitting attempts here. Rather, we consider it more useful to note that our model applies for case (II) (i.e., assuming nonspherical grains with distributed effective radius of curvature) and, allowing for the effects of initial porosity φ_i on contact stress enhancement, is successful in qualitatively predicting the trends seen in our experimental data, notably the effects of grain size and φ_i on stress-strain behavior. Amongst the alternatives considered, this model offers the best explanation for the behavior observed in our experiments and suggests that the positive effect of grain size on strain seen in our experimental data (and in previous compaction experiments on granular aggregates [e.g., Chuhan *et al.*, 2002, 2003; Hangx *et al.*, 2010; Liteanu *et al.*, 2012]) is most likely due to the grain-size-dependent departure from sphericity (i.e., surface asperity radius) assumed in this case of the model.

7. Conclusions

Uniaxial compaction experiments performed on sands at room temperature using an oedometer, at stresses up to 30 MPa and under dry and fluid-flooded conditions, have shown quasi-elastic loading behavior and permanent deformation caused by elastic grain contact distortion and grain failure. The results show a systematic increase in strain achieved, i.e., in measured compressibility, with increasing sand grain size, as well as increase in these quantities with increasing initial porosity. A microphysical model has been developed, describing grain distortion and failure/crushing in terms of Hertzian contact mechanics and linear elastic fracture mechanics, in an attempt to explain the observed compaction behavior of the sands tested. Assuming that sand samples can be modeled as a regular (simple cubic) pack of grains, two extreme cases of the model were explored: (I) spherical grains with distributed flaw size at failure and (II) nonspherical grains with distributed effective radius of surface curvature, characterizing contact asperity amplitude. Compaction simulations based on case (II) of the model offer the best agreement with the experimentally observed stress-strain behavior and with the effects of grain size upon this, suggesting that a grain-size-dependent departure from sphericity of the constituent grains is important in controlling the compaction behavior of sands.

Notation

a	radius of contact circle between two grains
c	flaw dimension
c_0	initial flaw dimension
c_f	flaw dimension at failure
d	mean grain size
E^*	effective Young's modulus; $\frac{1}{E^*} = \frac{(1-\nu_1^2)}{E_1} + \frac{(1-\nu_2^2)}{E_2}$
e_v	volumetric strain
F	total normal load transmitted between two grains
F_c	critical force at failure
k	Weibull scale parameter
K_I	mode I stress intensity factor
$K_{c,I}$	mode I critical stress intensity factor
L_0	initial sample length
ΔL	incremental change in sample length
m	Weibull modulus
m_a	sample mass
N_0	initial number of intact grains
n_N	cumulative number of failed grains
n_R	number of grains removed from a SH pack to increase its porosity
R	radius of curvature
R_r	relative radius of curvature; $\frac{1}{R_r} = \frac{1}{R_1} + \frac{1}{R_2}$
V_0	initial solid volume
ΔV	incremental change in solid volume
Y	dimensionless factor, $Y \approx 1.12$ for a single-ended edge crack

Greek Symbols

α	linear scaling factor
δ_{tot}	total elastic distortion
ζ	linear scaling factor
ν	Poisson's ratio
σ_0	normal stress at the center of the contact area
σ_{eq}	applied equivalent stress
σ_n	normal contact stress
σ_T	maximum tensile stress at the edge of the Hertzian contact
ϕ_i	initial porosity
η	linear scaling factor
ρ_m	density of the sample; 2.648 g/cm ³ for quartz

Acknowledgments

We thank the Associate Editor and two anonymous reviewers for their positive feedback and constructive criticism on the initial manuscript.

References

- Anthony, J. L., and C. Marone (2005), Influence of particle characteristics on granular friction, *J. Geophys. Res.*, *110*, B08409, doi:10.1029/2004JB003399.
- Antonellini, M. A., A. Aydin, and D. D. Pollard (1994), Microstructure of deformation bands in porous sandstones at Arches National Park, Utah, *J. Struct. Geol.*, *16*(7), 941–959.
- Atkinson, B. K. (1979), A fracture mechanics study of subcritical tensile cracking of quartz in wet environments, *Pure Appl. Geophys.*, *117*, 1011–1024.
- Atkinson, B. K., and P. G. Meredith (1989), Experimental fracture mechanics data for rocks and minerals, in *Fracture Mechanics of Rock*, edited by B. K. Atkinson, pp. 477–525, Academic Press, London, U. K.
- Aydin, A., R. I. Borja, and P. Eichhubl (2006), Geological and mathematical framework for failure modes in granular rock, *J. Struct. Geol.*, *28*(1), 83–98.
- Baud, P., P. Meredith, and E. Townend (2012), Permeability evolution during triaxial compaction of an anisotropic porous sandstone, *J. Geophys. Res.*, *117*, B05203, doi:10.1029/2012JB009176.
- Birch, F. (1966), Compressibility; elastic constants, in *Handbook of Physical Constants, Revised Edition*, edited by S. P. Clark Jr., pp. 97–173, The Geological Society of America Memoir, New York.
- Borg, I., M. Friedman, J. Handin, and D. V. Higgs (1960), Experimental deformation of St. Peter sand: A study of cataclastic flow, in *Rock Deformation—A Symposium*, edited by D. Griggs and J. Handin, pp. 133–191, Geological Society of America Memoir, Washington, D. C.
- Brzesowsky, R. H. (1995), Micromechanics of sand grain failure and sand compaction, PhD thesis, 180 pp, Utrecht University, Utrecht, Netherlands.
- Brzesowsky, R. H., C. J. Spiers, C. J. Peach, and S. J. T. Hangx (2011), Failure behavior of single sand grains: Theory versus experiment, *J. Geophys. Res.*, *116*, B06205, doi:10.1029/2010JB008120.
- Burley, S. D. (1986), The development and destruction of porosity within Upper Jurassic reservoir sandstones of the Piper and Tartan fields, outer Moray Firth, North Sea, *Clay Miner.*, *21*(4), 649–694.
- Chang, C. S. (1993), Micromechanical modeling of deformation and failure for granulates with frictional contacts, *Mech. Mater.*, *16*(1–2), 13–24.
- Chang, C. S., M. G. Kabir, and Y. Chung (1992), Micromechanics modeling for stress-strain behavior of granular soils. II: Evaluation, *J. Geotech. Eng.*, *118*(12), 1975–1992.
- Cheng, Y. P., Y. Nakata, and M. D. Bolton (2003), Discrete element simulation of crushable soil, *Geotechnique*, *53*(7), 633–641.
- Chester, J. S., S. C. Lenz, F. M. Chester, and R. A. Lang (2004), Mechanisms of compaction of quartz sand at diagenetic conditions, *Earth Planet. Sci. Lett.*, *220*, 435–451.
- Chuhan, F. A., A. Kjeldstad, K. Bjørlykke, and K. Høeg (2002), Porosity loss in sand by grain crushing—Experimental evidence and relevance to reservoir quality, *Mar. Pet. Geol.*, *19*(1), 39–53.
- Chuhan, F. A., A. Kjeldstad, K. Bjørlykke, and K. Høeg (2003), Experimental compression of loose sands: Relevance to porosity reduction during burial in sedimentary basins, *Can. Geotech. J.*, *40*(5), 995–1011.
- Cilona, A., P. Baud, E. Tondi, F. Agosta, S. Vinciguerra, A. Rustichelli, and C. J. Spiers (2012), Deformation bands in porous carbonate grainstones: Field and laboratory observations, *J. Struct. Geol.*, *45*, 137–157.
- Cox, S. J. D., and P. G. Meredith (1993), Microcrack formation and material softening in rock measured by monitoring acoustic emissions, *Int. J. Rock Mech. Min. Sci. Geomech. Abstr.*, *30*(1), 11–24.
- Darot, M., and Y. Gueguen (1986), Slow crack growth in minerals and rocks: Theory and experiments, *Pure Appl. Geophys.*, *124*(4–5), 677–692.
- Donaldson, E. C., G. V. Chilingarian, and H. H. Rieke (1995), Stresses in sediments, in *Subsidence Due to Fluid Withdrawal*, edited by G. V. Chilingarian et al., pp. 165–192, Elsevier Science, Amsterdam, Netherlands.
- Doornhof, D., T. G. Kristiansen, N. B. Nagel, P. D. Patillo, and C. Sayers (2006), Compaction and subsidence, *Oilfield Review* *18*, no. 3 (Autumn 2006): 50–68.
- Eichhubl, P., J. N. Hooker, and S. E. Laubach (2010), Pure and shear-enhanced compaction bands in Aztec Sandstone, *J. Struct. Geol.*, *32*(12), 1873–1886.
- Fossen, H., R. A. Schultz, and A. Torabi (2011), Conditions and implications for compaction band formation in the Navajo Sandstone, Utah, *J. Struct. Geol.*, *33*(10), 1477–1490.
- Gill, J. J., C. Miglionico, and M. Andrews (1990), Measurement of the microstructural response of lightly-cemented granular soils under uniaxial strain conditions, in *Micromechanics of Failure of Quasi-Brittle Materials*, edited by S. P. Shah et al., pp. 206–213, Elsevier Applied Science, London, U. K.
- Groshong, R. H. J. (1988), Low-temperature deformation mechanisms and their interpretation, *Geol. Soc. Am. Bull.*, *100*(9), 1329–1360.
- Gueguen, Y., T. Reuschlé, and M. Darot (1990), Single crack behaviour and crack statistics, in *Deformation Processes in Minerals, Ceramics and Rocks*, edited by D. J. Barber and P. G. Meredith, pp. 334–353, Unwin Hyman, London, U. K.
- Guimaraes, M. S., J. R. Valdes, A. M. Palomino, and J. C. Santamarina (2007), Aggregate production: Fines generation during rock crushing, *Int. J. Min. Process.*, *81*, 237–247.
- Hangx, S. J. T., C. J. Spiers, and C. J. Peach (2010), Creep of simulated reservoir sands and coupled chemical-mechanical effects of CO₂ injection, *J. Geophys. Res.*, *115*, B09205, doi:10.1029/2009JB006939.
- Harirechi, O., and G. R. McDowell (2003), Discrete element modelling of cyclic loading of crushable aggregates, *Granular Matter*, *5*, 147–151.
- Hettema, M., E. Papamichos, and P. M. T. M. Schutjens (2002), Subsidence delay: Field observations and analysis, *Oil Gas Sci. Tech.*, *57*(5), 443–458.
- Hicks, B. D. (1989), Dissolution of experimentally compacted quartz sand, PhD thesis, 266 pp, University of Missouri-Columbia, Columbia, Mo.
- Huber, M. T. (1904), Zur Theorie der Berührung fester elastischer Körper, *Ann. Phys.*, *319*(6), 153–163.
- Isichenko, M. B. (1992), Percolation, statistical topography, and transport in random media, *Rev. Mod. Phys.*, *64*(4), 961.
- Issa, J. A., and R. B. Nelson (1989), Numerical analysis of micromechanical behavior of granular materials, *Eng. Comput.*, *9*(2), 211–223.
- Johnson, K. L. (1987), *Contact Mechanics*, p. 464, Cambridge Univ. Press, Cambridge, U. K.
- Johnson, N. L., and S. Kotz (1970), *Continuous Univariate Distributions*, vol. 1, p. 300, John Wiley, New York.
- Karig, D. E., and G. Hou (1992), High-stress consolidation experiments and their geologic implications, *J. Geophys. Res.*, *97*(B1), doi:10.1029/91jb02247.
- Karner, S. L., J. S. Chester, F. M. Chester, A. K. Kronenberg, and A. Hajash (2005), Laboratory deformation of granular quartz sand: Implications for the burial of clastic rocks, *AAPG Bull.*, *89*(5), 603–325.
- King, G. C. P., and C. G. Sammis (1992), The mechanisms of finite brittle strain, *Pure Appl. Geophys.*, *138*(4), 611–640.
- Ko, H. Y., and R. F. Scott (1967), Deformation of sand in hydrostatic compression, *J. Soil Mech. Found. Div. Am. Soc. Civ. Eng.*, *93*(SM3), 137–156.
- Lambe, T. W., and R. V. Whitman (1979), *Soil Mechanics*, p. 553, SI Version, Wiley Eastern Limited, New Delhi, India.
- Lee, K. L., and I. Farhoomand (1967), Compressibility and crushing of granular soil in anisotropic triaxial compression, *Can. Geotech. J.*, *4*(1), 68–86.
- Liteanu, E., A. R. Niemeijer, C. J. Spiers, C. J. Peach, and J. H. P. De Bresser (2012), The effect of CO₂ on creep of wet calcite aggregates, *J. Geophys. Res.*, *117*, B03211, doi:10.1029/2011JB008789.

- Liu, Z., L. R. Myer, and N. G. W. Cook (1993), Micromechanics of granular materials—Numerical simulation of the effects of heterogeneities, *Int. J. Rock Mech. Min. Sci. Geomech. Abstr.*, 30(7), 1281–1284.
- Lockner, D. (1993), The role of acoustic emission in the study of rock fracture, *Int. J. Rock Mech. Min. Sci. Geomech. Abstr.*, 30(7), 883–899.
- Marone, C., and C. H. Scholz (1989), Particle-size distribution and microstructures within simulated fault gouge, *J. Struct. Geol.*, 11(7), 799–814.
- Maxwell, J. C. (1960), Experiments on compaction and cementation of sands, in *Rock Deformation: A Symposium*, edited by D. Griggs and J. Handin, pp. 105–132, The Geological Society of America Memoir, Washington, D. C.
- McDowell, G. R., and M. D. Bolton (1998), On the micromechanics of crushable aggregates, *Geotechnique*, 48(5), 667–679.
- Mehta, A. (1994), *Granular Matter—An Interdisciplinary Approach*, pp. 306, Springer, Berlin, Germany.
- Meredith, P. G., and B. K. Atkinson (1982), High-temperature tensile crack propagation in quartz: Experimental results and application to time-dependent earthquake rupture, *Earthquake Predict. Res.*, 1, 377–391.
- Milliken, K. L. (1994), The widespread occurrence of healed microfractures in siliciclastic rocks: Evidence from scanned cathodoluminescence imaging, in *Rock Mechanics Models and Measurements, Challenges From Industry*, edited by P. P. Nelson and S. E. Laubach, pp. 825–832, Balkema, Rotterdam, Netherlands.
- Mollema, P. N., and M. A. Antonellini (1996), Compaction bands: A structural analog for anti-mode I cracks in aeolian sandstone, *Tectonophysics*, 267, 209–228.
- Morey, G. W., R. O. Fournier, and J. J. Rowe (1962), The solubility of quartz in water in the temperature interval from 25° to 300°C, *Geochim. Cosmochim. Acta*, 26(10), 1029–1043.
- Niemeijer, A. R., C. J. Spiers, and B. Bos (2002), Compaction creep of quartz sand at 400–600°C: Experimental evidence for dissolution-controlled pressure solution, *Earth Planet. Sci. Lett.*, 195(3–4), 261–275.
- Nishizawa, O., and H. Noro (1990), A self-exciting process of acoustic emission occurrence in steady creep of granite under uniaxial stress, *Geophys. Res. Lett.*, 17, 1521–1524, doi:10.1029/GL017i010p01521.
- Oda, H., H. Koami, and K. Seya (1989), Effect of occurrence rate of acoustic emissions on their statistical behavior, *Pure Appl. Geophys.*, 130(1), 5–29.
- Onasch, C. M. (1994), Assessing brittle volume-gain and pressure solution volume-loss processes in quartz arenite, *J. Struct. Geol.*, 16(4), 519–530.
- Ouwerkerk, C. E. D. (1991), A micro-mechanical connection between the single-particle strength and the bulk strength of random packings of spherical particles, *Powder Tech.*, 65(1–3), 125–138.
- Papamichos, E., I. Vardoulakis, and H. Ouadfel (1993), Permeability reduction due to grain crushing around a perforation, *Int. J. Rock Mech. Min. Sci. Geomech. Abstr.*, 30(7), 1223–1229.
- Reuschlé, T. (1989), *Les fluides et l'évolution de propriétés mécaniques des roches*, PhD thesis, 378 pp., Université Louis Pasteur de Strasbourg, Strasbourg, France.
- Rice, J. R. (1992), Fault stress states, pore pressure distributions, and the weakness of the San Andreas Fault, in *Fault Mechanics and Transport Properties of Rocks—A Festschrift in Honor of W.F. Brace*, edited by B. Evans and T.-F. Wong, pp. 475–503, Academic Press, London, U. K.
- Rimstidt, J. D., and H. L. Barnes (1980), The kinetics of silica-water reactions, *Geochim. Cosmochim. Acta*, 44(11), 1683–1699.
- Roberts, J. E., and J. M. de Souza (1958), The compressibility of sands, *Proc. Am. Soc. Test. Mater.*, 58, 1269–1277.
- Robie, R. A., B. S. Hemingway, and J. R. Fisher (1978), Thermodynamic properties of minerals and related substances at 298.15 K and 1 bar (10^5 Pa) pressure and at higher temperatures, *US Geol. Surv. Bull.*, 1452, 451–456.
- Rustichelli, A., E. Tondi, F. Agosta, A. Cilona, and M. Giorgioni (2012), Development and distribution of bed-parallel compaction bands and pressure solution seams in carbonates (Bolognano Formation, Majella Mountain, Italy), *J. Struct. Geol.*, 37, 181–199.
- Schutjens, P. M. T. M. (1991), Experimental compaction of quartz sand at low effective stress and temperature conditions, *J. Geol. Soc.*, 148(3), 527–539.
- Segall, P. (1992), Induced stresses due to fluid extraction from axisymmetric reservoirs, *Pure Appl. Geophys.*, 139(3), 535–560.
- Shen, H. H., M. Satake, and M. M. Mehrabadi (1992), *Advances in Micromechanics of Granular Materials*, p. 476, Elsevier Science Publishers, Amsterdam, Netherlands.
- Simmons, G., and H. F. Wang (1971), *Single Crystal Elastic Constants and Calculated Aggregate Properties*, MIT Press, Cambridge, U. K.
- Skurtveit, E., A. Torabi, R. H. Gabrielsen, and M. D. Zoback (2013), Experimental investigation of deformation mechanisms during shear-enhanced compaction in poorly lithified sandstone and sand, *J. Geophys. Res. Solid Earth*, 118, 4083–4100, doi:10.1002/jgrb.50342.
- Stauffer, D., and A. Aharony (1992), *Introduction to Percolation Theory*, 2nd ed., Taylor and Francis, London, U. K.
- Sumino, Y., and O. L. Anderson (1984), Elastic constants of minerals, in *Handbook of Physical Properties of Rocks*, vol. III, edited by R. S. Carmichael, pp. 39–138, CRC Press, New York.
- Thornton, C. (Ed) (1993), *Powders and Grains*, vol. 93, p. 472, Balkema, Birmingham, Ala.
- Vesic, A. S., and G. W. Clough (1968), Behaviour of granular materials under high stresses, *J. Soil Mech. Found. Div. Am. Soc. Civ. Eng.*, 94(SM3), 661–687.
- Visser, H. J. M., C. J. Spiers, C. J. Peach, and S. J. T. Hangx (2012), Effects of interfacial energy on compaction creep by intergranular pressure solution: Theory vs. experiments on a rock analogue (NaNO_3), *J. Geophys. Res.*, 117, B11211, doi:10.1029/2012JB009590.
- Walther, J. V., and H. C. Helgeson (1977), Calculation of the thermodynamic properties of aqueous silica and the solubility of quartz and its polymorphs at high pressures and temperatures, *Am. J. Sci.*, 277(10), 1315–1351.
- Wang, B., Y. Chen, and T.-f. Wong (2008), A discrete element model for the development of compaction localization in granular rock, *J. Geophys. Res.*, 113, B03202, doi:10.1029/2006JB004501.
- Weibull, W. (1951), A statistical distribution function of wide applicability, *J. Appl. Mech.*, 18, 293–297.
- Wilson, J. C., and E. F. McBride (1988), Compaction and porosity evolution of Pliocene sandstones, Ventura Basin, California, *AAPG Bull.*, 72(6), 664–681.
- Wong, T.-f., and P. Baud (2012), The brittle-ductile transition in porous rock: A review, *J. Struct. Geol.*, 44, 25–53.
- Wong, R. C. K., W. E. Bar, and P. R. Kry (1993), Stress-strain response of Cold Lake oil sands, *Can. Geotech. J.*, 30, 220–235.
- Zallen, R. (1983), *The Physics of Amorphous Solids*, p. 320, John Wiley, New York.
- Zhang, J., T.-F. Wong, and D. M. Davis (1990a), Micromechanics of pressure-induced grain crushing in porous rocks, *J. Geophys. Res.*, 95(B1), 341–352, doi:10.1029/JB095iB01p00341.
- Zhang, J., T.-F. Wong, T. Yanagidani, and D. M. Davis (1990b), Pressure-induced microcracking and grain crushing in Berea and Boise sandstones: Acoustic emission and quantitative microscopy measurements, *Mech. Mater.*, 9(1), 1–15.
- Zhu, W., L. G. J. Montesi, and T.-f. Wong (1997), Shear-enhanced compaction and permeability reduction: Triaxial extension tests on porous sandstone, *Mech. Mater.*, 25(3), 199–214.
- Zoback, M. D., and J. D. Byerlee (1976), Effect of high-pressure deformation on permeability of Ottawa Sand, *AAPG Bull.*, 60(9), 1531–1542.